Boosting water flux and dye removal: Advanced composite membranes incorporating functionalized AC-PAA for wastewater treatment

Imran Ahmad Khan [a], Kashif Mairaj Deen [b,*], Edouard Asselin [b], Muhammad Yasir [c], Rehan Sadiq [d], Nasir M. Ahmad [a,*]

[a] School of Chemical and Materials Engineering (SCME), National University of Sciences and Technology (NUST), H-12 Sector, Islamabad 44000, Pakistan
[b] Department of Materials Engineering, The University of British Columbia, Vancouver V6T 1Z4, BC, Canada
[c] Centre of Polymer Systems, University Institute, Tomas Bata University in Zlin, Trida Tomase Bati 5678, 76001 Zlin, Czech Republic
[d] Department of Civil Engineering, School of Engineering, The University of British Columbia, Okanagan Campus, Kelowna V1V 1V7, BC, Canada

ARTICLE INFO

ABSTRACT

This study addresses the challenge of enhancing dye removal and antifouling properties in wastewater treatment by developing a composite membrane incorporating poly(acrylic acid)-functionalized activated carbon (AC-PAA) into a polyethersulfone (PES) matrix. The activated carbon was functionalized using surface-initiated atom transfer radical polymerization (SI-ATRP), followed by hydrolysis to introduce hydrophilic poly(acrylic acid) chains. The AC-PAA composite was characterized using Fourier transform infrared spectroscopy, thermogravimetric analysis, transmission electron microscopy, and energy-dispersive X-ray analysis, confirming successful grafting and functionalization. Compared to pristine PES, the addition of 0.5 wt% AC-PAA led to significantly enhanced water flux (54 L/m^{2}h vs. 30 L/m^{2}h) and superior dye removal, achieving 63 % for methyl orange and 67 % for methylene blue at alkaline pH. Poly(acrylic acid) was selected for its carboxyl groups, which enhance adsorption capacity and antifouling characteristics. In addition to effective dye removal, the composite membranes were antifouling, with a flux recovery ratio of 72 %. Response surface methodology optimized parameters, confirming highest performance at pH 11 and 6 bar. AC-PAA functionalized membranes are an efficient solution in wastewater treatment, increasing dye removal and antifouling capacity versus current membrane technologies.

Introduction

Water scarcity is a major global challenge exacerbated by the discharge of chemical and textile wastewater into natural reservoirs [1,2]. Emergent pollutants, such as dyes, pharmaceuticals, hydrazine, and heavy metals from various industrial sources, pose significant environmental threats, necessitating the development of efficient methods for their detection and removal [2,3]. To ensure industrial sustainability, wastewater must be treated and purified before being released into the environment. Emerging pollutants like dyes, pharmaceuticals, hydrazine, and heavy metals from industrial sources require effective removal to meet discharge standards [4]. While physical, chemical, and biological methods are commonly employed, chemical treatments are often costly, complex, and generate secondary waste requiring further disposal. Biological treatments are sensitive to environmental factors, such as temperature, pH, oxygen levels, and toxicity,

requiring precise control for optimal performance. In contrast, the physical methods are cost-effective, simple, and efficient for pollutant removal from wastewater [5]. Recently, metal–organic frameworks (MOFs), including heterometallic sodium-europium-clusters, group IIIA element based MOFs [6,7], and dimethyl 4-(carbaldehyde oxime) pyridine-2,6-dicarboxylate (L1), have attracted attention for their high sensitivity and efficiency in pollutant detection and removal [8]. However, MOFs face limitations, including complex and costly synthesis, as well as poor stability under harsh environmental conditions such as high humidity or extreme pH [9].

Compared to conventional methods such as distillation, adsorption, and liquid–liquid extraction, membrane-based separation offers superior scalability, robustness, and ease of integration into existing water treatment systems, making it highly practical for large-scale pollutant removal [10,11]. Over the past two decades, membrane technology has rapidly advanced, providing a versatile means of purifying materials in

various phases (solid, liquid, and gas) [12–14]. This progress is due to the development of both polymeric and inorganic membranes. Among polymeric options, polyether sulfone (PES) has become prominent, especially in nanofiltration, due to its excellent mechanical, thermal, and chemical resistance properties, as well as its stability across a wide pH range, making it ideal for harsh water treatment environments [15–17]. However, the hydrophobic nature of PES leads to organic fouling, reducing its lifespan. To improve performance, PES membranes require enhanced hydrophilicity [18,19]. Achieving a balance between hydrophilic and hydrophobic properties can improve their capacity to separate ions and organic compounds [20,21]. The incorporation of fillers like AC, carbon nanotubes, and graphene oxide has shown potential in enhancing membrane performance [22]. AC, in particular, is valued for its porous structure, large surface area, and versatility in various applications, including its use as a filler in membranes and filtration media [23–25]. However, achieving uniform dispersion of AC within the polymer matrix is challenging due to its poor dispersive properties. Surface modification of AC is necessary to improve dispersion, though current methods are limited by AC's abundant surface-active sites [26–29]. Therefore, new strategies for functionalizing AC are essential to fully optimize its use in water treatment applications.

Surface modification through polymer grafting is one of the most effective ways to change the characteristics and functionality of a surface [30]. Where the type and amount of polymer used in grafting determines the final surface properties. In surface-initiated atom-transfer radical polymerization (SI-ATRP), polymer chains are covalently attached to a material's surface via the "grafting from" process. This method allows precise grafting of polymers with specific structures and functional groups onto various substrates. SI-ATRP has recently been used to functionalize carbon-based materials like AC, carbon nanotubes, and graphene [29–33]. However, unexpected changes in AC surfaces due to SI-ATRP are rarely documented, with only a few cases, such as Liu et al.'s, [34] use of poly(hydroxyethyl acrylate) (PHEA) and Yahan Liu et al.'s [29] application of poly(methyl methacrylate) (PMMA). Further understanding of the polymerization properties and structure of modified AC is needed to produce variable surface characteristics for AC-based functional materials.

In most studies on composite membranes, inorganic additives like silicon dioxide and aluminum oxide are used [35]. Nevertheless, the addition of AC and its modified forms to organic polymers for creating composite membranes has not been widely explored. Mukerjee et al. [36] developed AC/cellulose acetate hybrid composite membranes and found that the extent of AC loading affected permeability and phenol removal efficiency. Low carbon loading resulted in high flux, while higher carbon loading increased phenol rejection rates. Peyravi et al. [37] found that functionalized aminated AC/PES hybrid composite membranes outperformed their non-functionalized counterparts. In these membranes, the presence of AC and AC-NH$_2$ decreased the mean pore size and increased porosity due to changes in the concentrations of solvent and nonsolvent phases during phase inversion. This enhanced porosity and the presence of hydrophilic functional groups increased the permeation flow in the PES membrane matrix. A comparable increase in membrane flux was attributed to the combined effect of high porosity and a large number of hydrophilic functional groups [37]. However, the flux remained at 7 kg.m^{-2}.h^{-1}, which is considered relatively low for practical industrial applications. To address the flux issue, a study by Makheta et al. [38] employed a different functionalized carbon-based material (graphene oxide) in a PES membrane, increasing water flux up to 140 L/m^2·h. However, the dye removal efficiency decreased to 60 % for MO and 20 % for MB. Hosseini et al. developed a mixed matrix PES membrane with AC nanoparticles for sulfate and copper ion removal, achieving 95 % and 97 % removal, respectively, with 0.5 wt% AC. However, water flux was low, reaching only 9 L/m^2/h at 0.1 wt% AC, and no optimization of operational parameters was undertaken [39]. Another study produced PES membranes with highly uniform AC spheres (HUACS) using ultrasonication-assisted dispersion, with the 0.5

wt% HUACS membrane achieving 85 % dye rejection but limited flux (5 wt% HUACS gave only 3 L/m^2/h), though it demonstrated strong anti-fouling properties with a 90 % flux recovery ratio [39]. Ghaemi et al. incorporated poly(sodium 4-styrenesulfonate)-coated multiwall carbon nanotubes (MWCNTs) into polysulfone membranes using RSM to optimize flux and dye removal, and finding that a 0.1 wt% MWCNT membrane achieved 13 L/m^2/h flux and 99 % dye removal. Results indicated acidic pH and moderate dye concentration favor dye removal, while basic pH and dilute dye solution maximize flux [40]. Consistently, studies report an inverse relationship between dye rejection and permeation flux, underscoring the importance of balancing these parameters in membrane development—a primary goal of this study.

Response Surface Methodology (RSM) has become essential for optimizing wastewater treatment processes. A recent study used RSM with Central Composite Design (CCD) to optimize a photocatalyst combining and graphitic carbon nitride (g-C$_3$N$_4$), achieving 98.3 % azo dye photodegradation from wastewater under sunlight. The RSM was used to identify an optimal GWW to g-C$_3$N$_4$ ratio (5 mL:0.5 g) [41]. Similarly, Muthukumar et al. developed a photocatalyst from hot dip galvanization waste and fly ash, achieving 98.3 % ciprofloxacin degradation under natural sunlight in 60 min. The photocatalyst had excellent reusability and an optimized electronic band structure. Using Box-Behnken design in RSM, the optimal degradation conditions were determined as 20 ppm ciprofloxacin, pH 4, 0.01 g photocatalyst loading, and 0.01 mL H$_2$O$_2$ [42].

In a study using the Taguchi method to optimize photocatalytic parameters for dye removal, reduced graphene oxide (rGO/TiO$_2$) photocatalysts achieved a 95 % MB removal at 80 ppm MB, 0.15 g catalyst loading, pH 8. The rGO matrix enhanced electron transfer, while TiO$_2$'s narrow bandgap improved photocatalytic efficiency, demonstrating the potential of rGO/TiO$_2$ for dye wastewater treatment [43]. Another study employed the RSM approach to optimize copper-doped galvanic waste-derived photocatalysts, achieving 63.7 % degradation of resin industry wastewater, closely matching the predicted 67.8 %—highlighting the value of predictive modeling for industrial wastewater treatment [44]. Gasemloo et al. [45] used RSM to optimize chromium removal with sulfated carboxymethyl cellulose membranes. Similarly, Momina et al. [46] applied RSM to predict flux in PES/chitosan/MWNTs membranes for salt removal, and He et al. optimized drinking water treatment sludge properties for enhanced performance. This approach aligns with the objective of our study in optimizing the performance of AC-PAA membranes for wastewater treatment [47]. Unlike previous studies, however, RSM has not yet been applied for MO and MB removal using functionalized AC membranes, highlighting the novelty of our current work.

Our research addresses the well-documented trade-off between dye rejection and flux in membrane technology, where enhancing dye rejection often reduces flux. The goal of this work is to design a membrane that simultaneously optimizes both, overcoming this efficiency limitation. Moreover, while many antifouling strategies focus solely on surface functionalization, leaving the membrane core vulnerable, our approach distributes antifouling properties throughout the membrane matrix by blending grafted additives (AC-PAA). This strategy mitigates fouling at the core, promotes stability, and ensures uniform performance over time.

The primary objective of this study is to develop and assess high-performance, pH-responsive polymer membranes for wastewater treatment, using grafted PAA on AC particles, created through SI-ATRP. These particles are incorporated into PES nanocomposite membranes via the phase inversion method. Membrane performance, including water flux, dye rejection, and fouling resistance, is evaluated alongside morphology and hydrophilicity tests. The use of RSM to optimize pH and transmembrane pressure underscores the innovative potential of these PAA-grafted AC membranes for effective wastewater treatment applications.

Materials and methods

Materials

AC was obtained from Merk (Germany) while other Chemicals and reagents of analytical quality were purchased from Sigma-Aldrich (Germany). The chemicals used included α-bromoisobutyl bromide (98 %), 3-aminopropyl trimethoxysilane (97 %) (APTMS), triethylamine (99.5 %), copper (I) bromide (CuBr, 98 %), PMDETA (N, N, N', N'', N''-pentamethyl diethylene triamine) (99 %), t-butyl acrylate (t-BA, 98 %), dichloromethane, and trifluoroacetic acid. Other chemicals including nitric acid (70 %), sulfuric acid (98 %), hydrochloric acid (37 %), sodium hydroxide (NaOH), acetone, and tetrahydrofuran (THF) were purchased from Sigma-Aldrich (Germany). For membrane preparation, polyether sulfone (PES) and N-methyl-2-pyrrolidone (NMP) were obtained from Ultrasone and Sigma-Aldrich (Germany), while polyvinylpyrrolidone (PVP) was supplied by Merck, Germany. The adsorbates, including methyl orange, methylene blue, and bovine serum albumin ($\geq$ 98 %) were obtained from Sigma-Aldrich (Germany). DI water was used where it was necessary throughout the experiments. Analytical-grade nitrogen gas was supplied by Linde Pakistan Limited.

Methods

Pretreatment of AC

During the pretreatment process (as described elsewhere [48]), the AC was washed with deionized water for 24 h and then dried at 110 °C in a vacuum oven. The mechanism of surface modification of the AC is illustrated in Fig. 1(a). First, 250 mg of washed AC was added to a 250 ml mixture of 3:1 (v/v) of nitric acid (HNO$_3$ 70 %) and sulfuric acid (H$_2$SO$_4$ 98 %) in a round-bottom flask. The flask was heated to 120 °C and refluxed for five hours with vigorous magnetic stirring. After refluxing, the AC solution underwent multiple centrifugation-based dilution and decantation cycles to raise the pH to 5. The AC was then dried overnight at 80 °C in a vacuum oven.

Synthesis of amine-functionalized activated carbon (AC-NH₂)

After pretreatment, the surface of the AC was modified with APTMS. The AC was dispersed through sonication in tetrahydrofuran (0.1 mg mL^{-1}) for 1 h at room temperature. APTMS (AC: APTMS, 1:10) was added to this evenly distributed mixture and heated at 70 °C for 15 h. The excess APTMS was removed by filtering and washing the mixture with Tetrahydrofuran (THF) multiple times before drying it for 48 h in a vacuum oven. This modified carbon sample is referred to as AC-NH$_2$ and is presented in Fig. 1(a).

Initiator attachment over APTMS-functionalized AC

The initiator attachment onto amine-functionalized activated carbon (AC-NH$_2$) through a controlled surface modification process is shown in Fig. 1(b). Initially, 1.5 g of AC-NH$_2$ was dispersed in 50 mL of dichloromethane within a round-bottom flask equipped with a magnetic stirrer. To neutralize acidic byproducts and maintain an optimal pH, 0.5 mL of triethylamine was added. The flask was then cooled in an ice-water bath to 0 °C, which controlled the reactivity during the acylation step, minimizing side reactions and ensuring uniform functionalization. Once at the desired temperature, 20 mL of dichloromethane and
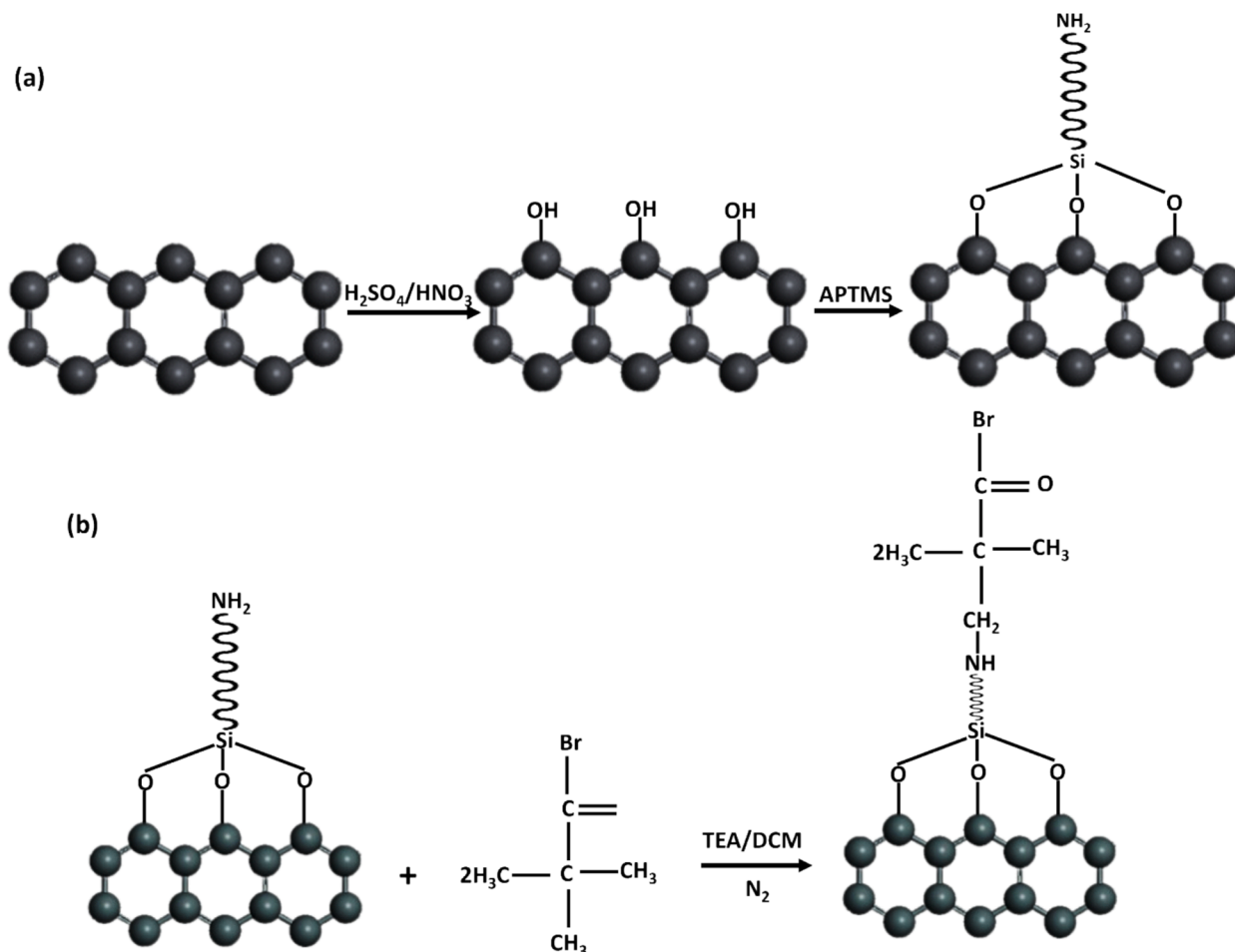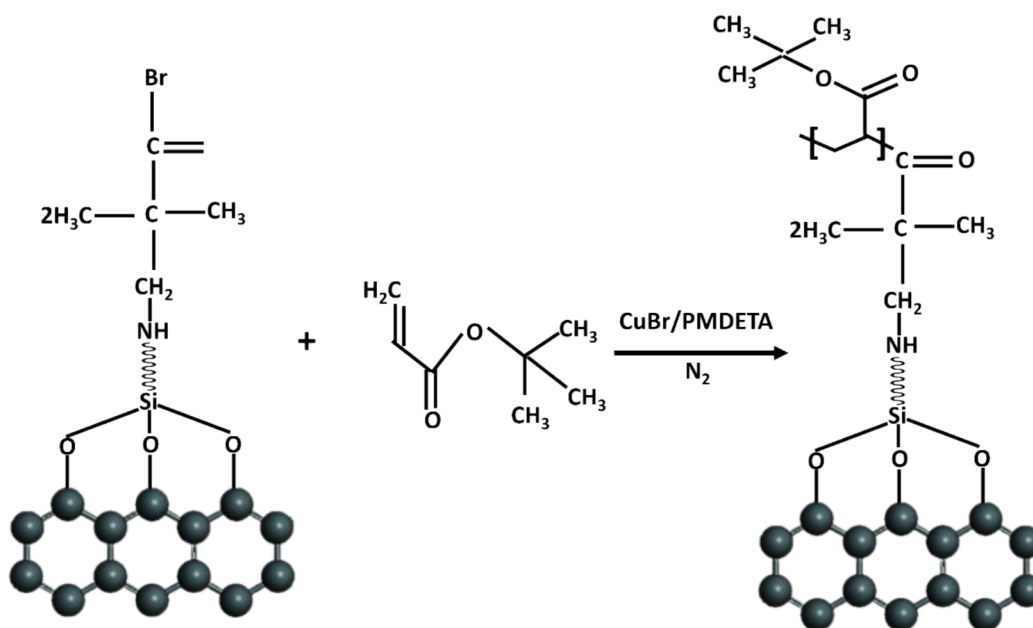

Fig. 1. Schematic showing the (a) pretreatment (b) Initiator attachment over AC-NH$_2$ to AC-NH-Br, (c) Growth of P(t-BA) brushes, and (d) Hydrolysis of AC-P(t-BA) to AC-PAA.
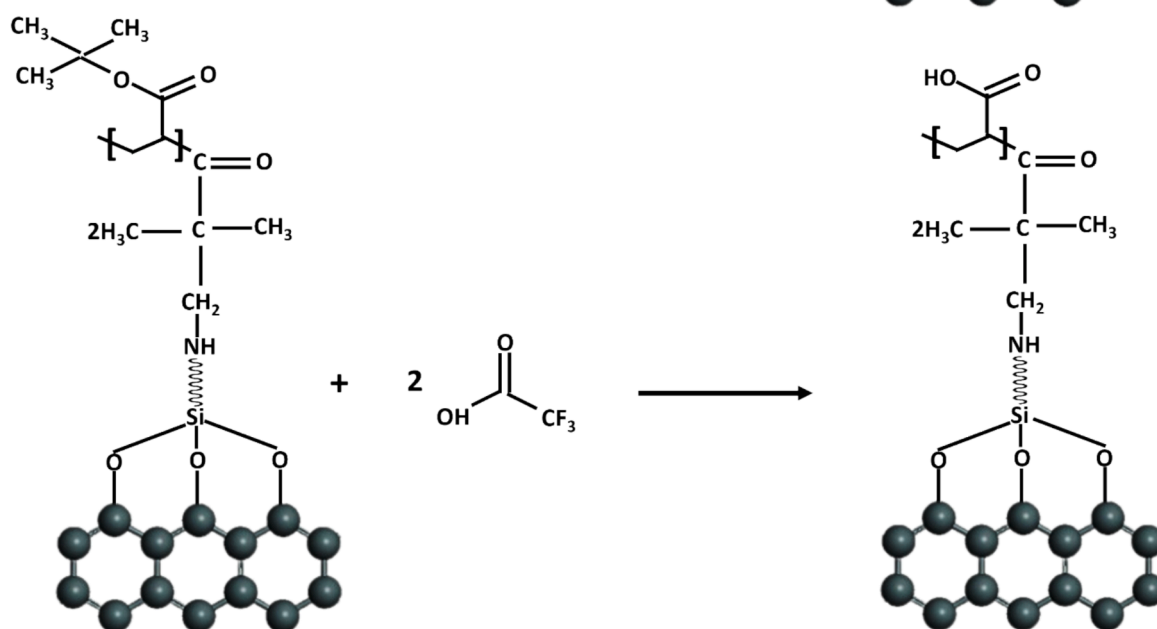
(c)

(d)

Fig. 1. (*continued*).

2 mL of α-bromoisobutyl bromide were added dropwise to control reagent addition and reduce exothermic reactions. The mixture was stirred for 30 min at 0 °C to facilitate nucleophilic substitution for initiator attachment, followed by a 48-hour reaction period at room temperature to ensure complete reaction of α-bromoisobutyl bromide with the AC-NH_2 groups. Afterward, the functionalized product, AC-NH-Br, was isolated via filtration, thoroughly washed with acetone and deionized water to eliminate unreacted reagents and byproducts and dried at 40 °C in a vacuum oven to remove residual solvents while preventing thermal degradation of the functional groups. The successful attachment of the initiator was confirmed through characterization using FTIR and elemental analysis.

Growth of P(t-BA) on AC surface

In the subsequent step, 60 mg of PMDETA, 5 mL of *tert*-butyl acrylate (the monomer), and 90 mg of CuBr (the catalyst) were added to a 10-mL glass vial containing AC-NH-Br. The vial was heated to 60 °C in an oil bath and stirred at 300 rpm for 24 h to promote atom transfer radical

polymerization (ATRP). This temperature was chosen to enable controlled polymerization of the monomer onto the surface of the activated carbon, with CuBr and PMDETA ensuring catalytic efficiency and reaction stability throughout the process. After polymerization, the functionalized activated carbon was washed with THF to eliminate unreacted monomers and residual catalyst. The final product was dried in a vacuum oven at 40 °C for four hours. The resulting material, labeled as AC-P(t-BA), was subsequently confirmed through FTIR analysis, as illustrated in Fig. 1(**c**).

Hydrolysis of AC-P(t-BA) to AC-PAA

Following the grafting of P(t-BA), the product underwent hydrolysis, as illustrated in Fig. 1(**d**). To achieve this, 40 mL of dichloromethane (DCM) and 1.5 mL of trifluoroacetic acid (TFA) were added to a flask, and AC-P(t-BA) was stirred in this solution for 30 min. After the hydrolysis reaction, the product was filtered, washed with DCM, and dried in a vacuum oven at 40 °C for four hours, resulting in AC-PAA. Each modification step, including the hydrolysis, was confirmed through

ATR-FTIR analysis to ensure successful functionalization of the AC.

Preparation of composite membranes

The phase inversion method was employed to fabricate membranes using PES sourced from BASF. In preparing the composite membranes, specific proportions of fillers, including pristine AC and AC-PAA, were incorporated into the PES polymer matrix. The composite membrane compositions, varying in concentrations of AC and AC-PAA, are designated as M0 to M6, as detailed in Table 1. This table specifies the concentrations and types of fillers used in each membrane sample, providing a comprehensive overview of the formulation for each membrane variant.

After grafting P(t-BA) onto the AC and its subsequent hydrolysis to AC-PAA, the phase inversion method was employed to fabricate the composite membranes. The process started with dissolving PES polymer and polyvinylpyrrolidone (PVP), a pore-forming agent, in 1-methyl-2-pyrrolidone (NMP). The total polymer concentration was maintained at 20 wt%, and the mixture was vigorously stirred for 24 h at 65 °C to ensure a well-dispersed solution. Following this, AC and AC-PAA were separately dispersed in the solvent and stirred overnight. These dispersions were then added to the polymer solution. The final mixture was cast onto a polyester support using an Automatic Film Applicator (Moderner AFA-IV, Shanghai Modern Instrument, China) at a speed of 5–6 mm/s. The cast solution was immediately immersed in a coagulation bath containing water (acting as an anti-solvent) maintained at 18 ± 1 °C for 4–5 min to complete the phase inversion process and form the nanocomposite membrane. To preserve the pores and membrane structure post-phase inversion, the membranes were submerged in a water and isopropanol (70/30) mixture for 19 h, followed by preservation in glycerol. The membrane during the casting stage of the phase inversion process is schematically shown in Fig. 2.

Characterization

The functional groups and elemental composition of AC and PAA-AC were characterized using ATR-FTIR (BRUKER Model ALPHA II, USA) and Energy Dispersive Spectroscopy (EDS) (Z2-i7 AMETEK, USA). Thermogravimetric analysis (TGA) was conducted using a Setaram TGA-DSC EVO instrument (France) under a nitrogen (N_2) atmosphere. The heating rate was set at 10 °C/min, and the analysis was carried out over the 20 to 800 °C temperature range. X-ray diffraction (XRD) analysis of AC and AC-PAA was performed using a Bruker D2 PHASER (Germany). The morphology of the AC and PAA polymer-grafted AC was examined using transmission electron microscopy (TEM) (Philips Model: CM200, USA). The morphology and structure (surface and cross-sectional) mixed matrix composite membranes were examined with a scanning electron microscope (SEM), (JEOL-JSM-6490LA) operating at 10–20 kV.

Water contact angle

To evaluate the hydrophilicity of the composite membranes prepared with AC and AC-PAA, the contact angle of the membrane surface was measured using the sessile drop method (using DSA-25, KRUSS analyzer). This method involves gently dropping 1 µL of water onto the top surface of the membrane and measuring the contact angle formed by the water droplet. The contact angle measurements were performed three times for each membrane, and the average value was calculated to minimize experimental errors and provide a representative hydrophilicity assessment.

Permeation tests

The permeability test was conducted to verify the hydrophilicity of the composite membrane in terms of measuring the water flux. Circular membranes with an effective surface area of 12 mm^2 were used throughout all the tests, facilitated by a Spider High throughput Membrane Testing Module (Model SP40, Belgium), which was connected to a nitrogen cylinder as shown in Fig. 3. During the test, distilled water served as feed solution, and the membrane was subjected to an external pressure of 8 bar. Permeation flux (J) was calculated using equation (1), which typically relates the volume of permeate (V) collected, the effective membrane area (A), and the duration of operation (t) [49].

$$J = \frac{V}{A.t} \tag{1}$$

Porosity

Porosity was determined through gravimetric analysis utilizing equation (2). Initially, the membranes were dried at 50 °C for 3 h to eliminate any residual moisture, and their weight (W_d) was recorded. Subsequently, these dried membranes were immersed in water at room temperature for 24 h. Following this soaking period, the membranes were extracted from the water, excess water was carefully removed with a Kim wipe, and their wet weight (W_w) was measured. The average membrane porosity was calculated using the equation (2) [50]:

$$\varepsilon = \frac{W_w - W_d}{A \times l \times d_w} \tag{2}$$

Where, W_d (dry mass before soaking) and W_w (wet mass after soaking) are the masses of membrane samples, in kg. "A" is the effective area of the membrane in m^2, dW is the water density in kg/m^3, and *l* is the thickness of the membrane (m).

Dye removal tests

Methylene blue (MB) and methyl orange (MO), chosen for their distinct characteristics, were used to evaluate the performance of the nanocomposite membranes. Table 2 provides details on these dyes, including characteristics and structural information. The selection of both positively and negatively charged dyes allows for studying how dye charge affects the filtration process. In the experiments, prepared membrane samples were employed to conduct dye removal studies of methylene blue (MB) and methyl orange (MO). The filtration tests were conducted under an applied pressure of 8 bar using a dead-end filtration cell assembly. The absorption intensity of the dye solutions before and after filtration was measured using a UV Visible Spectrophotometer (AE-S90 series, A&E Lab, UK). This method allows for quantifying the effectiveness of the membranes in removing both positively and negatively charged dyes from water. The rejection percentage for the removal of the dye was calculated using Equation (3) [51]:

$$R\% = \left(1 - \frac{C_P}{C_R}\right) \times 100 \tag{3}$$

Where R represents the rejection factor (%), Cp is the dye (MO and MB) concentration in the permeate (ppm), and C_R is the dye (MO and MB) concentration in the feed solution (ppm).

Table 1
Preparation of composite membranes – addition of various amounts of AC and AC-PAA (wt. %).

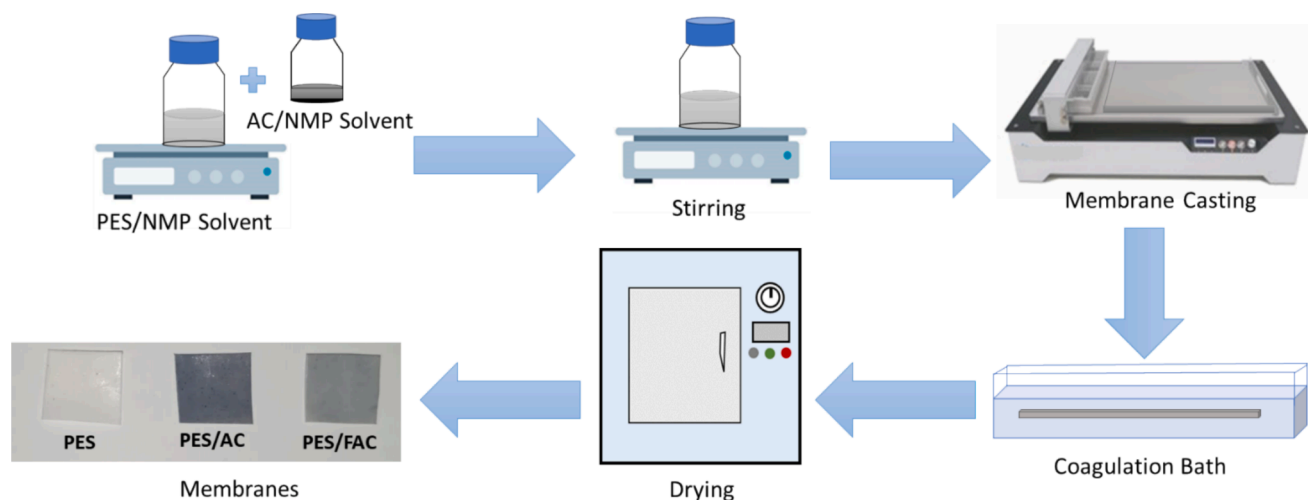| Sample	NMP solvent (%)	PES (%)	PVP (%)	AC (%)	AC-PAA (%)
M0	79	20	1	0	––
M1	78.9	20	1	0.1	––
M2	78.5	20	1	0.5	––
M3	78	20	1	1	––
M4	78.9	20	1	––	0.1
M5	78.5	20	1	––	0.5
M6	78	20	1	––	1

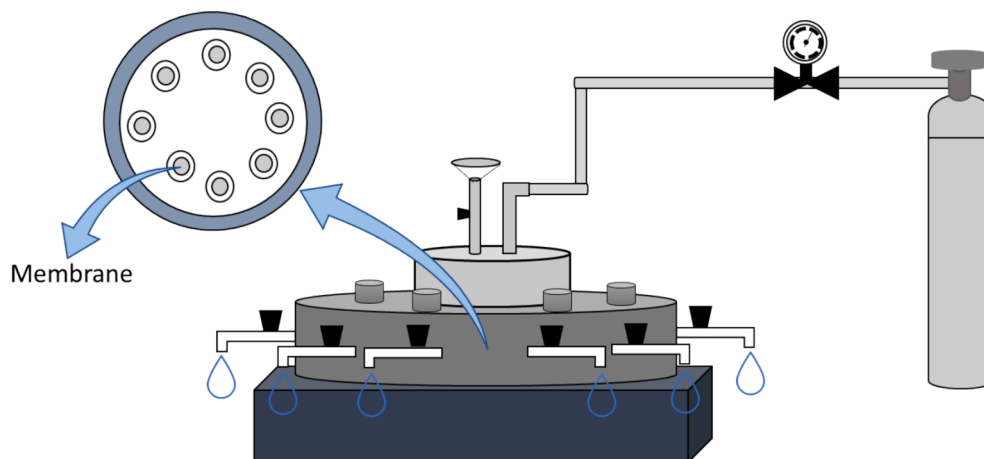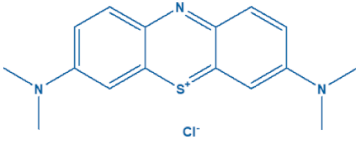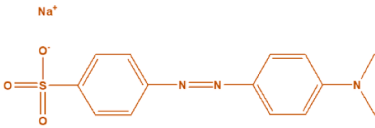**Fig. 2.** Schematic diagram showing the membrane fabrication process via the phase inversion method.

Fig. 3. Schematic of the HT Spider Membrane Testing Module for measuring the water flux through the membrane samples.

Table 2
Chemical structures of dyes used in this study.

Component	Structure	Charge	Molar weight ($gmol^{-1}$)	λ_{max} (nm) [Ref]
Methylene blue (MB)		+1	319.85	664 [52]
Methyl orange (MO)		−1	327.33	464 [53]

Fouling tests

The membrane sample sized at 12 mm^2 was used in the tests conducted with the high throughput membrane testing module in dynamic mode. Initially, the pure water flux (J_{w1}) was measured at a pressure of 8 bar. Subsequently, the module was filled with BSA solution (100 ppm), and the protein flux was monitored under the same pressure conditions. After completing the protein filtration, the membrane samples were washed, and the pure water flux (J_{w2}) was measured again. The flux recovery ratio (FRR) was calculated using Equation (4):

$$FRR\% = \frac{Jw_2}{Jw_1} \tag{4}$$

Results and discussion

ATR-FTIR, thermal and XRD analysis of modified AC

The IR spectrum of the AC initially shows no discernible peak pattern, indicating the absence of major functional groups (Fig. 4(a)). However, after modification to AC-NH$_2$, new peaks appear i.e., a

prominent peak at 1558 cm^{-1} indicating C = N presence, and another at 1480 cm^{-1} was assigned to the N–H group. In the 1000–1350 cm^{-1} region, peaks related to C–C stretching in aromatic rings and C-N stretching were observed [37,54]. Upon replacing AC-NH$_2$ with AC-Br using an initiator, the disappearance of certain peaks confirms the bonding of Br molecules to the surface. Peaks around 3400 cm^{-1} and 2900 cm^{-1} indicated alkyl stretching, while a peak at 1722 cm^{-1} represents the C = O group [55,56]. These results indicate the successful polymerization of tBA and the formation of tBA brushes on the AC surface. As shown in Fig. 4(b), after hydrolysis to form AC-PAA, the IR spectrum showed a characteristic peak at 1711 cm^{-1}, corresponding to the C = O functional group in PAA, and a broad peak indicative of the hydroxyl group spanning 2800 to 3600 cm^{-1} [57]. These ATR-FTIR results conclusively demonstrate the success of the "grafting from" technique in attaching PAA onto the AC surface, altering its chemical composition as intended.

Fig. 4(c) illustrates the thermogravimetric analysis (TGA) profiles of AC and AC-PAA, indicating significant differences in their thermal degradation behaviors. For AC, the initial weight loss begins at 30 °C, with the maximum weight loss occurring between 100 °C and 250 °C. This weight loss, approximately 7 % within this temperature range, is primarily attributed to the evaporation of water and moisture content [58]. Overall, AC demonstrates exceptional thermal stability, enduring temperatures up to 800 °C with a total weight loss of only 16 %.

In contrast, the TGA of AC-PAA reveals a three-step degradation process. The first decomposition stage (I), occurring between 50 °C and 200 °C, is attributed to the loss of absorbed water. The second decomposition stage (II), observed within the range of 300 °C to 400 °C, corresponds to the dehydration and decarboxylation of the polymer. The third decomposition stage (III), above 400 °C, represents the final degradation of the polymer [59,60]. The difference in weight loss observed at temperatures exceeding 400 °C between AC and AC-PAA implies that the quantity of PAA grafted onto AC-PAA was approximately 59 wt%.

The XRD analysis of pristine AC (Fig. 4(d)) reveals two broad peaks, observed at 20° and 35°, along with several narrow peaks between 40° and 45° [61]. The broadness of these peaks confirms a disordered graphite-like structure, indicative of amorphous carbon [62]. Following surface functionalization of AC with PAA, the XRD spectrum shows a single broad peak spanning 15° and 30°, which is characteristic of polyacrylic acid polymers [63]. Notably, the grafting process does not introduce any new crystalline peaks, suggesting that the composite structure remains predominantly amorphous after modification.

Surface morphology of AC and AC-PAA

The SEM images in Fig. 5 reveal distinct surface features of the AC before and after modification. In Fig. 5(a), the micrograph of pristine AC showed an external surface with visible cracks, holes, and crevices. Numerous sub-micrometer particles cover the AC surface, along with distinct cleavages and finer brighter particles, likely representing the ash fraction commonly found in commercial AC.

Fig. 5(b) displays the surface morphology of AC-PAA, where increased roughness was evident due to the grafting of PAA on the
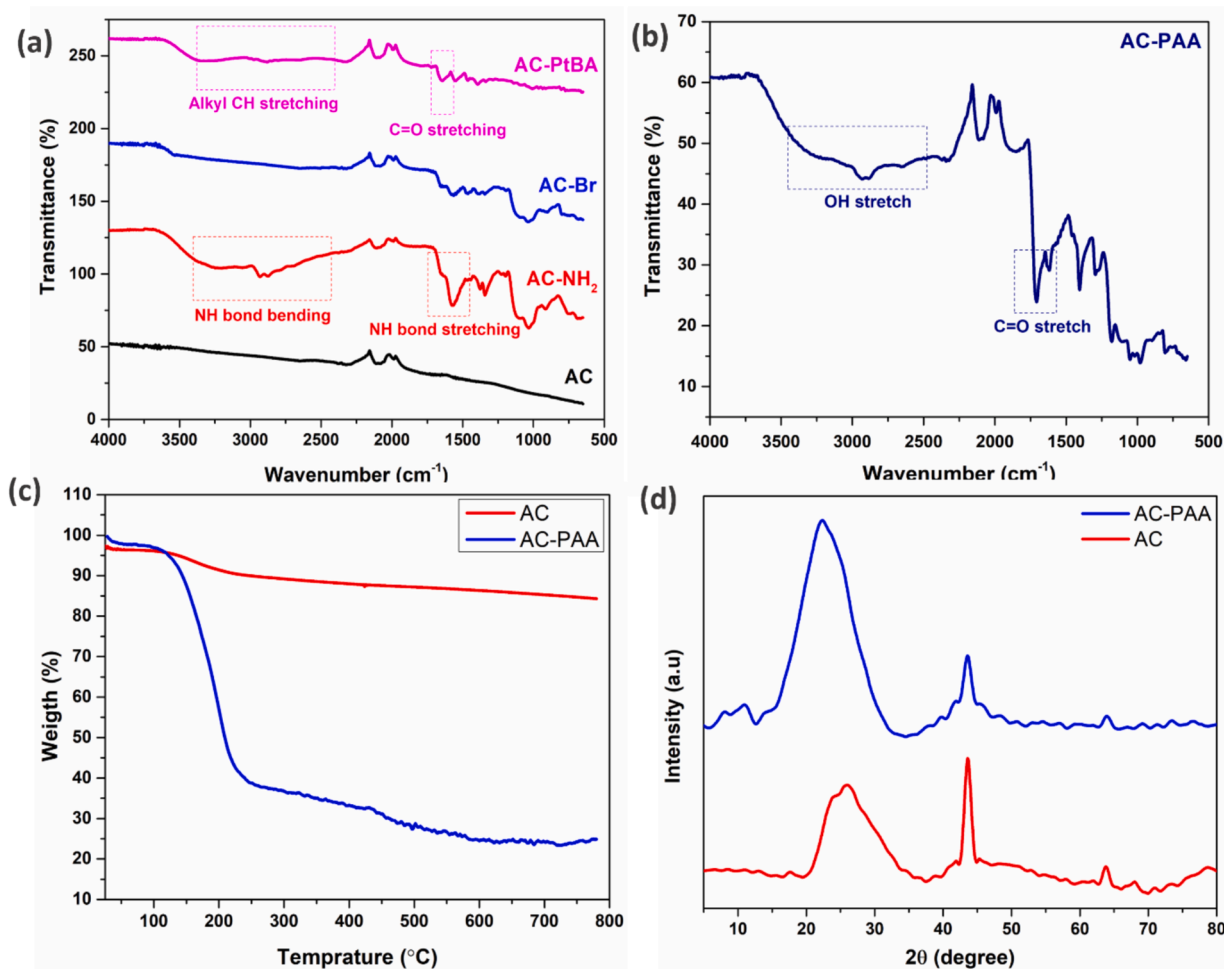

Fig. 4. ATR-FTIR Spectra of (a) AC, AC-NH$_2$, AC-Br, AC-PtBA, and (b) grafted AC with PAA and (c) Thermogravimetric analysis (TGA) curves of AC and AC-PAA, and (d) XRD spectra of pristine AC and AC-PAA.
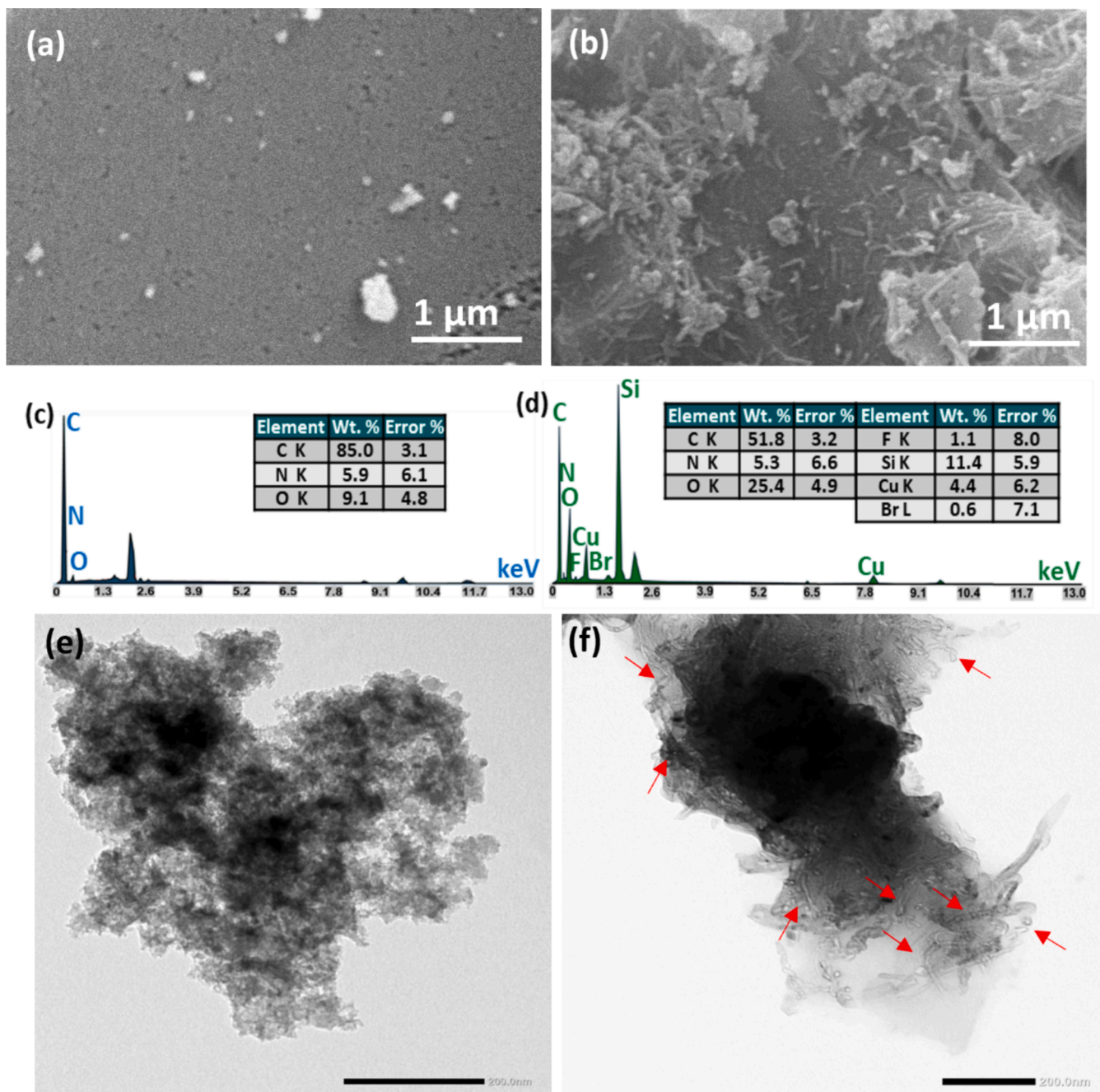
Fig. 5. Surface morphology of (a) pristine AC (b) AC-PAA; EDX spectra of (c) pristine AC and (d) AC-PAA; TEM images of (e) pristine AC, and (f) AC-PPA.

surface. The SEM analysis clearly shows needle-like structures indicative of PAA brushes protruding from the AC surface. The growth of PAA brushes enhances the surface roughness of AC, which is beneficial for improving water flow characteristics. Moreover, these morphology observations support the effective grafting density of polymer brushes on the surface on the modified AC surface, influencing critical parameters both in the dry conditions, such as surface roughness, and in wet conditions, such as surface wettability and water flux rates [37].

Energy dispersive X-ray spectroscopy (EDX) results for AC and AC-PAA are shown Fig. 5(c) and (d). Initially, the EDX analysis of AC reveals the presence of carbon (85 %), oxygen (9.1 %), and Nitrogen (5.9 %) as indicated in Fig. 5(c). These elements are characteristic of untreated AC. The EDX analysis of AC-PAA confirms the successful attachment of PAA to the AC surface. The analysis showed the presence of carbon (51.8 %), oxygen (25.4 %), nitrogen (5.3 %), fluorine (1.1 %),

silicon (11.4 %), copper (4.4 %), and bromine (0.6 %) (Fig. 5(d)). The significant increase in the oxygen content is attributed to the incorporation of PAA onto the AC surface, altering its elemental composition as intended [64]. This EDX analysis provides direct evidence of the chemical modification achieved through the grafting process.

Fig. 5(e) shows the TEM image of pristine AC, highlighting its microstructure, which consists of disordered carbon layers with a highly porous structure that includes both micro- and mesopores [65,66]. This porous structure is essential for applications requiring high surface area, as it facilitates greater interaction with functional materials. Fig. 5(f) illustrates the distribution of grafted PAA polymer chains, which appear to be randomly dispersed across the AC surface, indicating successful and uniform surface functionalization. The presence of PAA chains on the carbon surface not only enhances hydrophilicity but also introduces pH responsiveness, enabling the composite material to swell or shrink

based on the surrounding pH [55]. These TEM observations confirm the effective grafting of PAA, indicating that the functionalization process has modified the AC surface while maintaining its inherent porosity and disordered structure.

Morphology of the composite membranes

The introduction of AC and AC-PAA significantly altered the morphology of the composite membrane. For instance, with an increase in AC or AC-PAA concentration to 0.5 %, the formation of well-defined channel structures was evident in their sub-porous layer, as shown in Fig. 6(**a**), (**b**), (**d**), and (**e**). However, at a low concentration (0.1 % AC or AC-PAA), a relatively expanded porous layer with broader and partially closed-end channels was formed. This effect is associated with the accelerated diffusion of solvent from the casting solution to the coagulation bath during the fabrication process, resulting in the generation of finger-like voids [42]. At a 0.5 % AC or AC-PAA concentration, the relatively fine and well-oriented channel structure indicated the optimum concentration of AC/AC-PAA in the composite membrane (Fig. 6 (**b**) and **6**(**e**)). It was evident that with the addition of the optimum AC-PAA concentration, the morphology of the porous sublayer could be tuned by modifying the exchange rate between the solvent and nonsolvent phases during the precipitation stage, thus enhancing the effective interaction between the membrane casting solution and AC-PAA. As a result, the development of a well-defined and highly dense porous structure with fine voids containing walls can be ensured [28]. However, at higher AC and AC-PAA concentrations (1 %), due to an increase in the overall viscosity of the casting solution, the separation between the solvent and non-solvent phases was hindered, resulting in the formation of a membrane with a low porosity structure as shown in Fig. 6(**c**) and (**f**) [43].

Comparison of water flux, contact angle and porosity of the composite membranes

As shown in Fig. 7(**a**), the AC-PAA membranes had significantly better water flux compared to both pristine and AC/PES membranes. Specifically, the hydrophilic M5 membrane demonstrated a pure water permeation flux increase from 30 to 54 L/m^{2}h, nearly doubling the flux observed for the PES membrane. This improvement is much greater than that seen in modified PES membranes. The enhanced water flux in the AC-PAA membrane aligns well with its dense porous structure (Fig. 6(**e**)) and availability of a large number of hydrophilic active sites (–OH functional group) [67]. In contrast to the pristine PES membrane (M0), the PES membranes incorporated with non-functionalized AC content showed a moderate increase in water flux to 41 L/m^{2}h, despite the increase in the porosity of the M2 membrane (shown in Fig. 7(**b**) and discussed below). However, increasing the content of AC and AC-PAA up to 1 % resulted in decreased water flux i.e. M3 and M6 provided water fluxes of 37 and 49 L/m^{2}h, respectively. This decline is attributed to particle agglomeration at higher concentrations (>0.5 %), which led to aggregation and pore blockage.

The water flux analysis and contact angle measurements validated the improvement in the performance of AC and AC-PAA containing membranes. For example, compared to pristine PES membrane (M0), with the addition of AC into the PES membranes, the water contact angle reduced from 79° (without AC) to 63°, 58° and 60° for M1 (0.1 % AC), M2 (0.5 % AC), and M3 (1 % AC) membranes, respectively as shown in Fig. 7(**a**). These results indicated an increase in their hydrophilicity with the addition of AC. However, compared to pristine AC containing membranes, further augmentation in the hydrophilicity (reduction in the water contact angle) was observed in the presence of AC-PAA. At optimum concentration of AC-PAA (0.5 %), a significant reduction in the contact angle to 40° by the M5 membrane was specifically associated with the PAA functional groups (e.g., –COOH) on the surface of the AC-PAA/PES membranes. Further increase in the AC or AC-PAA concentration > 0.5 % resulted in the decrease of surface wettability as exhibited by the M3 and M6 membranes. This adverse effect was due to the aggregation of both AC and AC-PAA particles and the formation of a complex fine cellular morphology of the membrane during the synthesis process. This aggregation can negatively impact the porous structure of the membrane, reducing the accessibility of hydrophilic moieties to the membrane surface and thereby decreasing surface wettability [43]. Based on these results, it is evident that incorporating the optimum concentration of AC-PAA can modify the porous structure, improve water flux, and increase the hydrophilicity of the membrane.

Fig. 7(**b**) shows the variations in the porosity of the membrane samples. Without the addition of AC and AC-PAA, the PES membrane had the lowest porosity at 32 %. A slight increase in porosity to 40 %, 54 %, and 52 % was observed with the addition of AC, represented by the M1, M2, and M3 membranes, respectively. These results are consistent with the observed porous structure and water contact angle of the
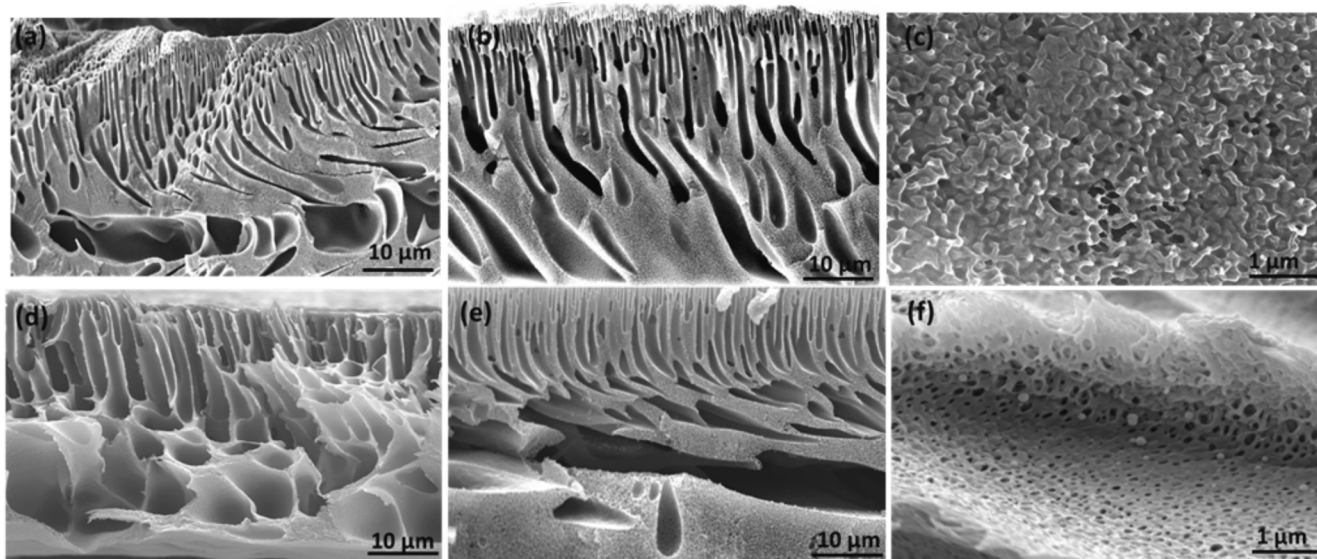

Fig. 6. SEM images showing the cross-sectional view of the composite membranes: (a) M0 (b) M2 (0.5% AC), (c) M3 (1% AC), (d) M4 (0.1% AC-PAA), (e) M5 (0.5% AC-PAA), and (f) M6 (1% AC-PAA).
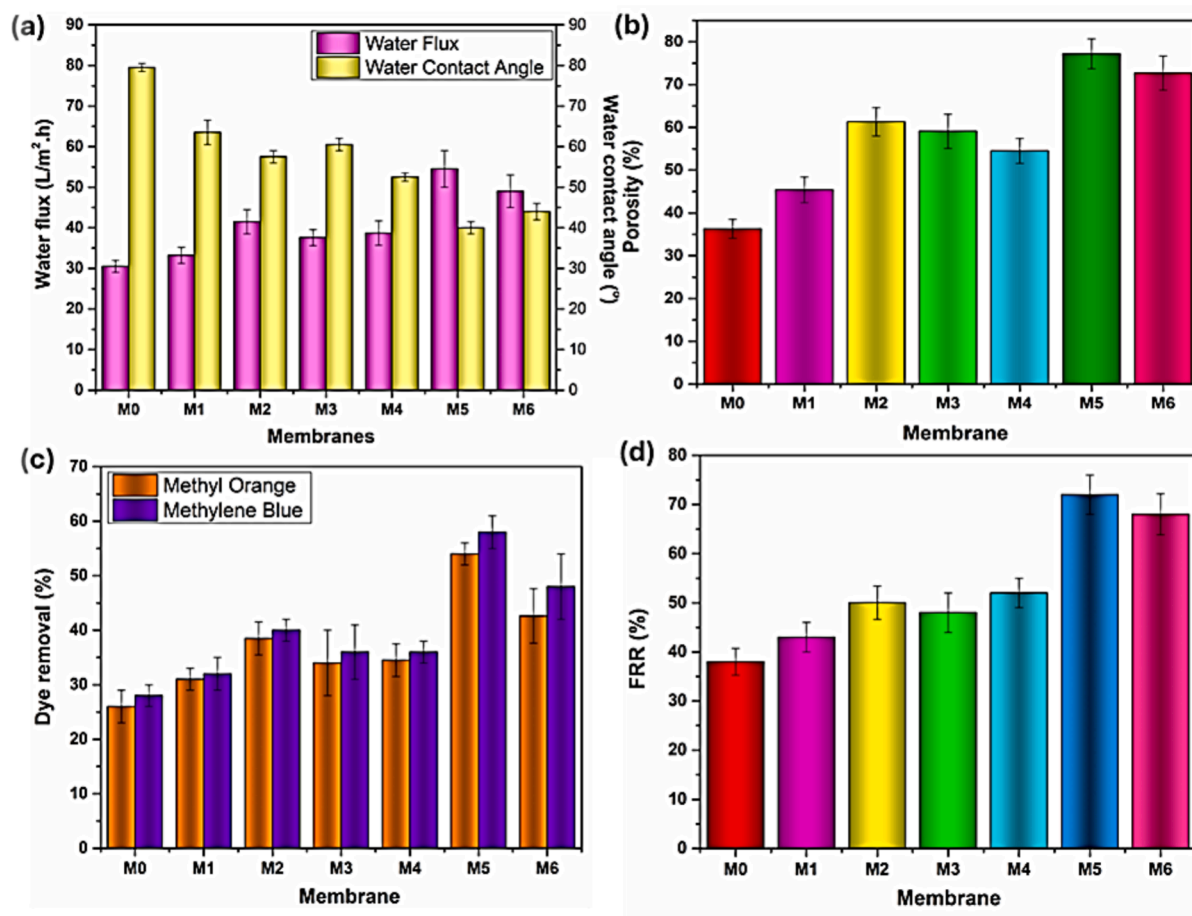
Fig. 7. (a) illustrates the variation in water flux and contact angle, while (b) compares the porosity of each composite membrane with that of M0 (PES without the addition of AC or AC-PAA) c) dye removal of the developed composite membranes, and d) anti-fouling characteristics of the composite membranes measured via dynamic fouling tests.

membrane samples. AC can disrupt the surface tension of the PES casting solution, facilitating the formation of a porous structure. The highest porosity of 68 % was obtained by the M5 membrane sample. This increase in porosity is attributed to the presence of AC-PAA in the casting solution, which promotes the formation of larger, open finger-like pores during the phase inversion process, particularly in the sublayer of the membrane. This finding validates that the addition of hydrophilic AC-PAA to the casting solution enhances the interchange between the solvent and non-solvent phases, resulting in the formation of a highly hydrophilic porous structure with improved water flux [39,68].

Dye removal efficiencies of the composite membranes

To test the dye rejection efficiency of the membranes, absorption data for each dye solution sample passed through the "Dead End Filtration Cell Assembly" were acquired using a UV–Visible Spectrophotometer. Fig. 7(c) presents the rejection extents of MO and MB dyes for all nanocomposite membranes. The pristine PES membrane showed low dye removal, with 26 % for MO and 28 % for MB. In contrast, the M2 membrane achieved 38.5 % MO removal and 40 % MB removal, while the M5 membrane had the highest efficiency with 54 % MO removal and 58 % MB removal. The dye rejection levels increased as the filler percentage rose from 0.1 % to 0.5 %. However, a decrease in dye removal was evident in 1 % AC or AC-PAA containing membranes. This optimal distribution at 0.5 % results in better interaction with dye molecules. At this concentration, the polymeric matrix is well-dispersed with AC and AC-PAA particles, leading to maximum dye rejection rates.

Two primary factors contributed to the enhanced dye removal

efficiency of the composite membranes. First, the high specific surface area and effective dye adsorption capability of AC played a crucial role in the performance of the composite membranes, as the large surface area and intricate pore structure of AC particles made them highly effective for filtration [46]. Second, the functional groups on the AC-PAA-containing membranes further improved the removal efficiencies for MB and MO dyes. These functional groups enabled not only electrostatic interactions but also hydrogen bonding, Van der Waals forces, and π–π interactions [47].

Also, the higher rejection of MB compared to MO is due to the positive charge of MB, which enhances adsorption on the negatively charged membrane surfaces, especially in membranes containing AC-PAA. In contrast, MO rejection is reduced due to repulsive interactions between the negatively charged dye and membrane surface, preventing its adsorption [48].

Anti-fouling characteristics of the composite membranes

Fig. 7(**d**) shows the dynamic test results for the fabricated membranes, where the flux recovery ratio (FRR) values indicated the recovery of flux after washing. Higher FRR values mean better antifouling characteristics. The FRR value for the pristine PES membrane was 38 %. However, incorporating 0.5 % AC-PAA in the M5 membrane increased the FRR to 72 %. Protein fouling occurred due to its deposition on the adsorbed monolayer, referred to as "reversible fouling," where proteins are lightly attached to the membrane surface and can be removed by washing [69]. Consequently, the water flux of the membranes is lower after BSA compared to the initial flow.

A hydrophilic functional group (–OH) reduces the attraction between the membrane and the BSA foulant by creating a hydration layer on the membrane, which hinders foulant attachment to the membrane surface [70,71]. This supports the trend of increased antifouling properties in the AC-PAA containing membranes. It is evident that increasing the amount of AC-PAA in the membrane structure raised the FRR percentage, peaking at 72 % with the addition of 0.5 % of AC-PAA, before dropping slightly to 68 % at higher AC-PAA concentration (1 %). This decline in FRR % is likely due to increased surface roughness of the membrane, a fact supported by other studies [72].

Effect of pressure and pH on membrane performance

The impact of various pressures (6, 8, and 10 bar) on the pure water flux was investigated for all membranes. As shown in Fig. 8(**a**), compared to the M0 (pristine PES) membrane, the pure water flux of the composite membranes increased linearly with increasing trans-membrane pressure. This linear dependence indicated the stability of the PES membrane structure due to high network crosslinking and the addition of hydrophilic fillers, i.e., AC and AC-PAA [54]. As discussed above, at all applied pressure values, the M5 membrane presented higher water flux compared to all other composite membranes. This behavior was associated with surface functional groups that improved the hydrophilicity of the 0.5 wt% AC-PAA containing membranes [55]. Despite the increased pressure, M5 maintained a higher water flux, demonstrating its improved performance and structural stability.

On the other hand, the incorporation of AC-PAA in membranes improved the water flux, which was strongly affected by the solution pH. For instance, the highest water flux of $\sim$ 60 L/m$^2 \cdot$h was achieved by the 0.5 % AC-PAA containing membrane (M5) at pH 3 and decreased substantially with an increase in solution pH. At low pH, the development of hydrogen bonds among the –COOH functional groups of PAA grafted AC led to the collapse of polymer chains, promoting the formation of open channel pores within the membrane [56,57].

When assessing the extent of dye removal under different pressures, the pristine (M0) membrane showed lower MO removal than M5. The

higher removal of the M5 membrane was attributed to the optimal distribution of AC-PAA within the PES matrix, which facilitated dye adsorption and interaction within the membrane matrix. However, increasing pressure leads to a slight reduction in MO removal. According to Fig. 8(**b**) and (**c**), for pristine PES and AC-PAA containing membranes, the higher pressure negatively impacts their removal for MO and MB dyes by allowing fewer dye molecules to interact with the membrane, possibly due to decreased dye/membrane interaction time. Approx. 55 and 60 % removal for MO and MB, respectively, were achieved at 6 bar pressure and decreased linearly with increase in pressure.

As shown in Fig. 8(**d**), increasing the pH from 3 to 7 had a negligible effect on the pure water flux through the pristine membrane (M0). Also, the addition of AC in PES slightly improved water flux; and these membranes (M1, M2 and M3) were less pH sensitive and provided almost constant water flux at all pH values. In contrast, a significant decrease in water flux was observed for the M5 membranes. At pH 3, the development of hydrogen bonds among the –COOH groups of PAA grafted on the AC surface led to the polymer chains collapsing, which opened the membrane pore size and increased the pure water flux. In an alkaline environment, hydrolysis of the acid groups caused the polymeric chains on the AC surface to expand, partially obstructing the pores and reducing the water flow through the membranes [58]. The mechanism of pH responsive behavior of AC-PAA containing PES membranes is schematically shown in Fig. 9(**b**) and (**c**).

The effect of pH on the removal of MO and MB dyes from M0 and M5 membranes was also examined, as shown in Fig. 8(**e**) and (**f**). The M0 membrane had a negligible effect of pH on the MO and MB removal efficiencies. The M5 membrane had a higher rejection of both MO and MB dyes compared to the M0 membrane, especially under alkaline conditions, due to increased electrostatic interactions. At pH 11, the polar carboxylic functional groups on the AC-PAA increased their interactions with water molecules. This enhanced electrostatic interaction between the polar functional groups on the dyes and the carboxylic groups on the AC-PAA improved dye rejection under alkaline conditions [59].

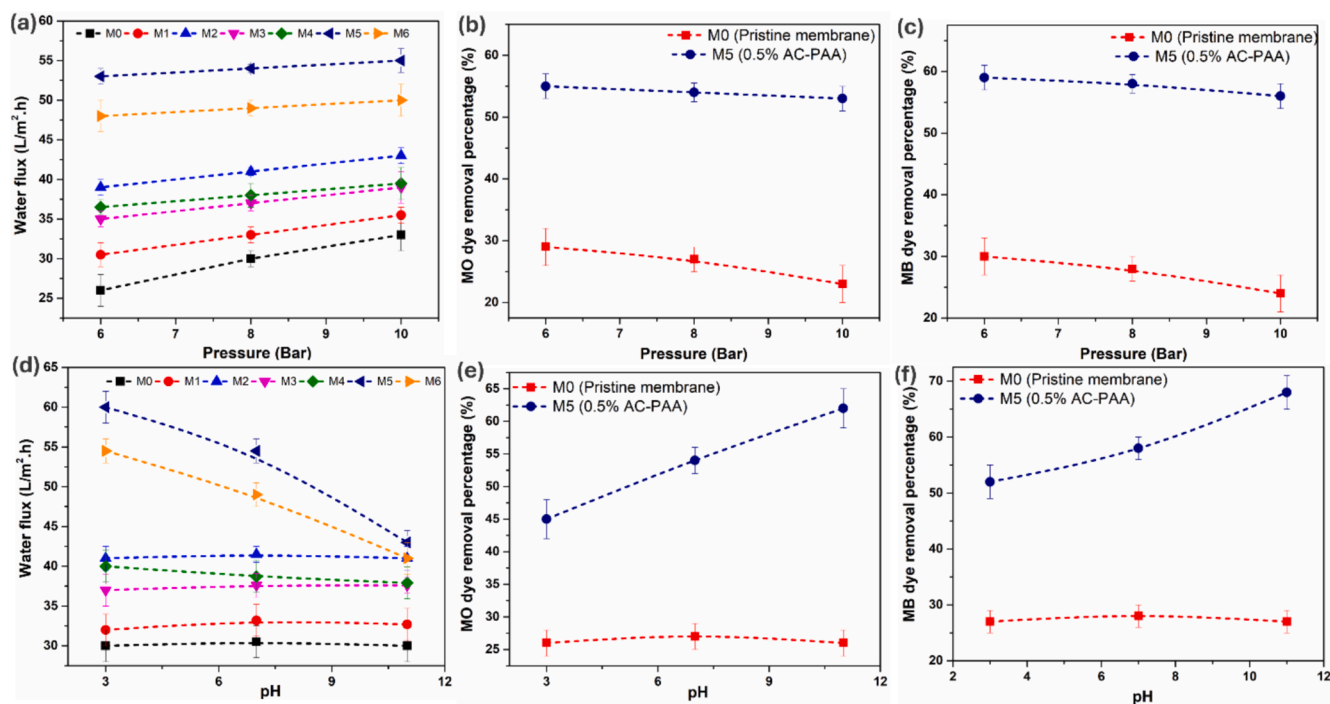The adsorption mechanism of MO and MB by AC-PAA is shown in

Fig. 8. The effect pressure on (a) the water flux capabilities of membranes. Comparison of pristine PES and M5 membranes for (b) MO and (c) MB removal. Water flux through composite membranes, the effect of (d) pH. Comparison of pristine PES and M5 membranes, removal efficiencies of (e) MO and (f) MB dyes as a function of pH.
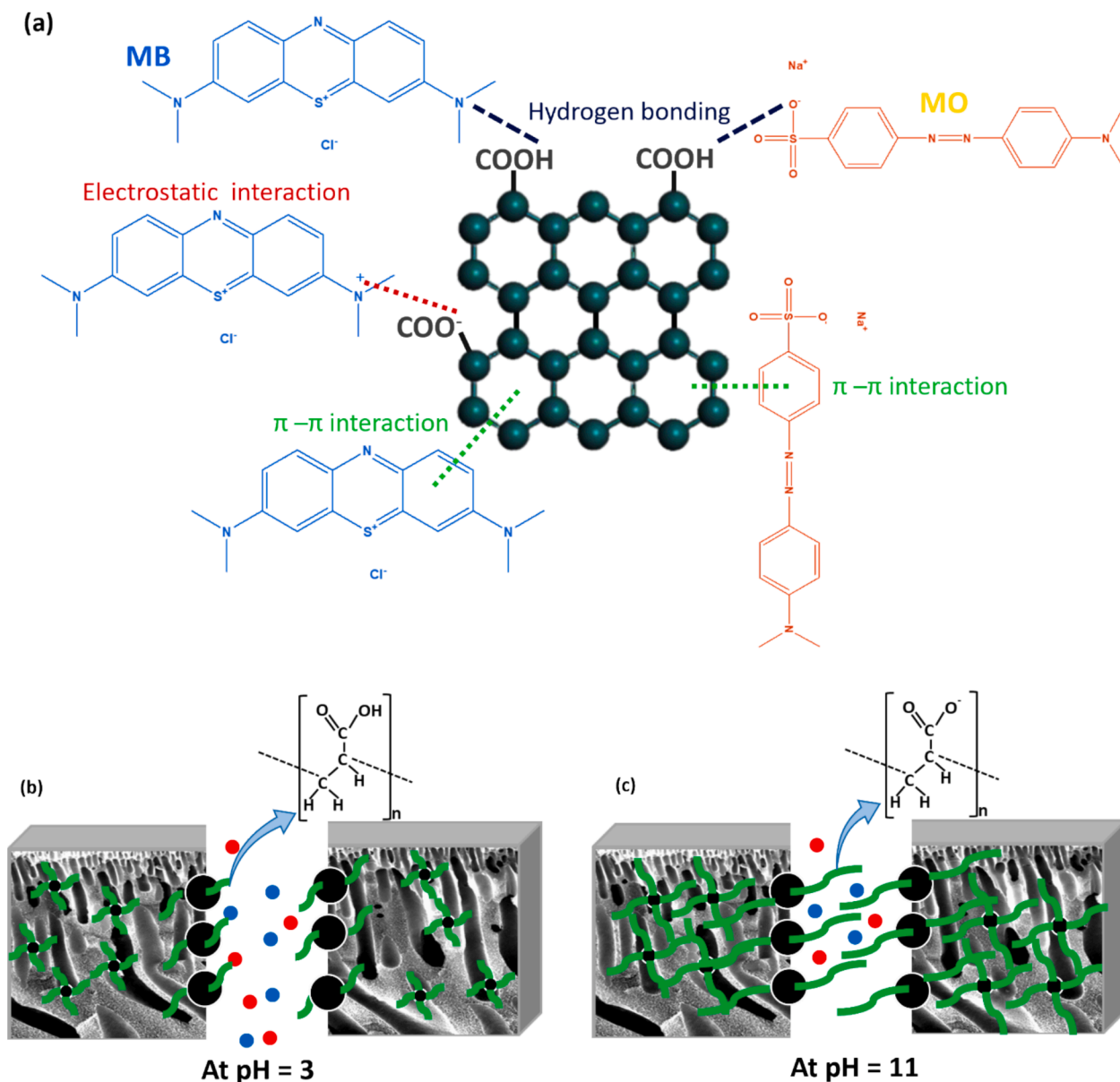
Fig. 9. (a) Adsoprtion mechanism of MO and MB on the AC-PAA (b) pH-responsive membranes at pH 3 and (c) pH 11.

Fig. 9(**a**). Both dyes feature π-conjugated backbones, which facilitate interaction with AC-PAA through π-π bond interactions (as summarized in Table 2) [73]. MO consists of two aromatic rings linked by an azo (−N = N-) bond, whereas MB has three aromatic rings arranged in a planar configuration. This structural difference suggests that the π-π interactions between MB and the aromatic rings of AC-PAA are likely more robust than those between MO and AC-PAA, resulting in a greater removal for MB than for MO [39]. Additionally, the numerous carboxyl groups present in AC-PAA can form hydrogen bonds with both dyes. For MO, hydrogen bonding can occur between the –COOH groups of AC-PAA and the oxygen atoms in the sulfonate (−SO$_3$) group of MO. In the case of MB, hydrogen bonds may form between the nitrogen or sulfur heteroatoms in its aromatic structure and the –COOH groups of AC-PAA, as illustrated in Fig. 9(**a**) [73]. Furthermore, the surface of AC-PAA carries a negative charge (due to the – COO$^-$ functional group) across a broad pH range [74]. This leads to a significantly higher removal capacity for MB compared to MO.

Statistical analysis and RSM modeling of MO and BSA removal

Design-Expert Software (DX 10) version 13 was employed for statistical analysis. The results obtained from the analysis of variance (ANOVA) were used to evaluate the variation between the experimental parameters (pH and pressure) and the modeling response of the M5-modified membrane. The input parameters and responses for MO and MB removal by the M5-modified membrane are listed in Table 3. Equations (5–6), established through regression analysis, provide the correlations between the input parameters and their effect on the MO removal percentage, representing the solution pH and the applied pressure by the variables A (pH) and B (pressure). The correlation coefficient (R^2), calculated using regression analysis, estimates the accuracy of the created models. R^2 values close to 1 indicate a strong correlation between the predicted and observed values, confirming the model's predictability. For the M5-modified membrane, the R^2 values were 0.99 for MO removal and 0.98 for MB removal (Table 4). The Model F-values of 82.45 (MO) and 42.73 (MB) imply that the models are significant, with only a 0.01 % (MO) and 0.04 % (MB) chance that such

Table 3

ANOVA analysis – the effect of experimental variables on the removal efficiencies of MO and MB by M5 membrane.

Runs	A(pH)	B(Pressure)	MO removal %	MB removal %
1	3	6	46	53
2	11	6	63	67
3	1.4	8	41	45
4	7	8	54	58
5	3	10	43	51
6	7	11	52	55
7	7	8	54	58
8	7	8	54	58
9	11	10	60	65
10	7	5	56	60
11	12.5	8	59	63
12	3	6	46	53
13	11	6	63	67
14	1.4	8	41	45

large F-values could occur due to noise. P-values less than 0.05 indicate significant model terms; both A and B were significant for MO and MB. Values greater than 0.1 indicate non-significant model terms.

For MO, the Predicted R^2 of 0.91 is in reasonable agreement with the adjusted R^2 of 0.98 (the difference is less than 0.2). For MB, the Predicted R^2 of 0.84 is in reasonable agreement with the Adjusted R^2 of 0.95 (the difference is less than 0.2). Therefore, these models can be used to navigate the design space effectively. A high p-value for lack of fit (LOF) in Table 4 quantifies the residual and pure error within the experimental domain based on data from replicated experimental designs. This value must be insignificant, as was the case in the study, indicating a good fit.

$$MO\ removal\ percentage\ (\%) = 54 + 9.2A - 1.46B + 0.125A^2 - 0.375B^2 \tag{5}$$

$$MB\ removal\ percentage\ (\%) = 58 + 8.7A - 1.63B - 0.5AB + 0.812A^2 - 0.062B^2 \tag{6}$$

As illustrated in Fig. 10(**a**) and (**b**), a linear relationship was observed between the predicted and experimental (actual) percentage removal values of MO and MB by the M5-modified membrane. The direct correlation between the experimental and projected responses confirmed the accuracy of the statistical modeling.

Fig. 10(**c**) and (**d**) illustrate the combined effect of pressure and pH on the removal of MO and MB dyes by the M5-modified membrane. While the applied pressure has a minor impact on its performance due to the stability of its structure, changes in pH significantly influenced the

removal of both dyes. Fig. 10(**c**) shows the impact of pH and initial solution pressure on the adsorption efficiency for MO. The data indicates that higher pH levels and lower pressure conditions enhanced removal. Specifically, as pH increases from 3 to 11 while maintaining a constant pressure of 6 bar, the removal improves from 46 % to 63 %.

A similar trend is observed for MB removal in Fig. 10(**d**). The removal increased from 51 % to 69 % as pH increased from 3 to 11. These findings underscore the significant role of pH in optimizing dye removal efficiency for the M5-modified membrane. Table 5 presents the optimal processing parameters for the removal of MO and MB, as determined by the RSM modeling. The verification run demonstrated close agreement with the predictions: the actual MO removal was 63 %, compared to the predicted value of 64 %, resulting in a margin of error of just 1 %. Similarly, the actual MB removal was 67 %, with only a 2 % margin of error from the predicted value of 69 %.

Comparison of water flux and dye rejection by AC-PAA/PES with other membranes

Table 6 compares the performance of PES membranes integrated with various carbon-based materials in terms of flux rate and dye removal efficiency. This comparison shows that adding carbon-based materials improves the membrane's flux and dye removal performance. The AC-PAA containing PES membranes developed in this study have a balanced performance. They offer a flux rate of 54 L/m2·h, which is higher than several other membranes but lower than the highest reported flux rates (e.g., 140 L/m2·h for Cu(terephthalate acid (tpa) GO/PES). In terms of dye removal, AC-PAA/PES membranes achieve 63 % for MO and 67 % for MB. This balanced performance is notable because it combines a competitive flux rate with substantial dye rejection, setting it apart from other membranes that either excel in flux rate but have lower dye removal (e.g., Cu(terephthalate acid (tpa) GO/PES)) or vice versa (e.g., PES/Functionalized MWCNTs)). In summary, this moderate flux and dual-dye removal capacity suggests that the AC-PAA/PES membrane is advantageous for applications needing both reasonable throughput and efficient dye filtration, benefitting from the hydrophilic, pH-responsive nature of PAA.

Conclusion

Poly (acrylic acid) (PAA) was successfully grafted onto the surface of activated carbon (AC) via surface-initiated atom transfer radical polymerization (SI-ATRP). Initially, poly(t-butyl acrylate) chains were grafted onto the AC surface through SI-ATRP, followed by hydrolysis to

Table 4

Analysis of variance (ANOVA) test for the removal of MO and MB.

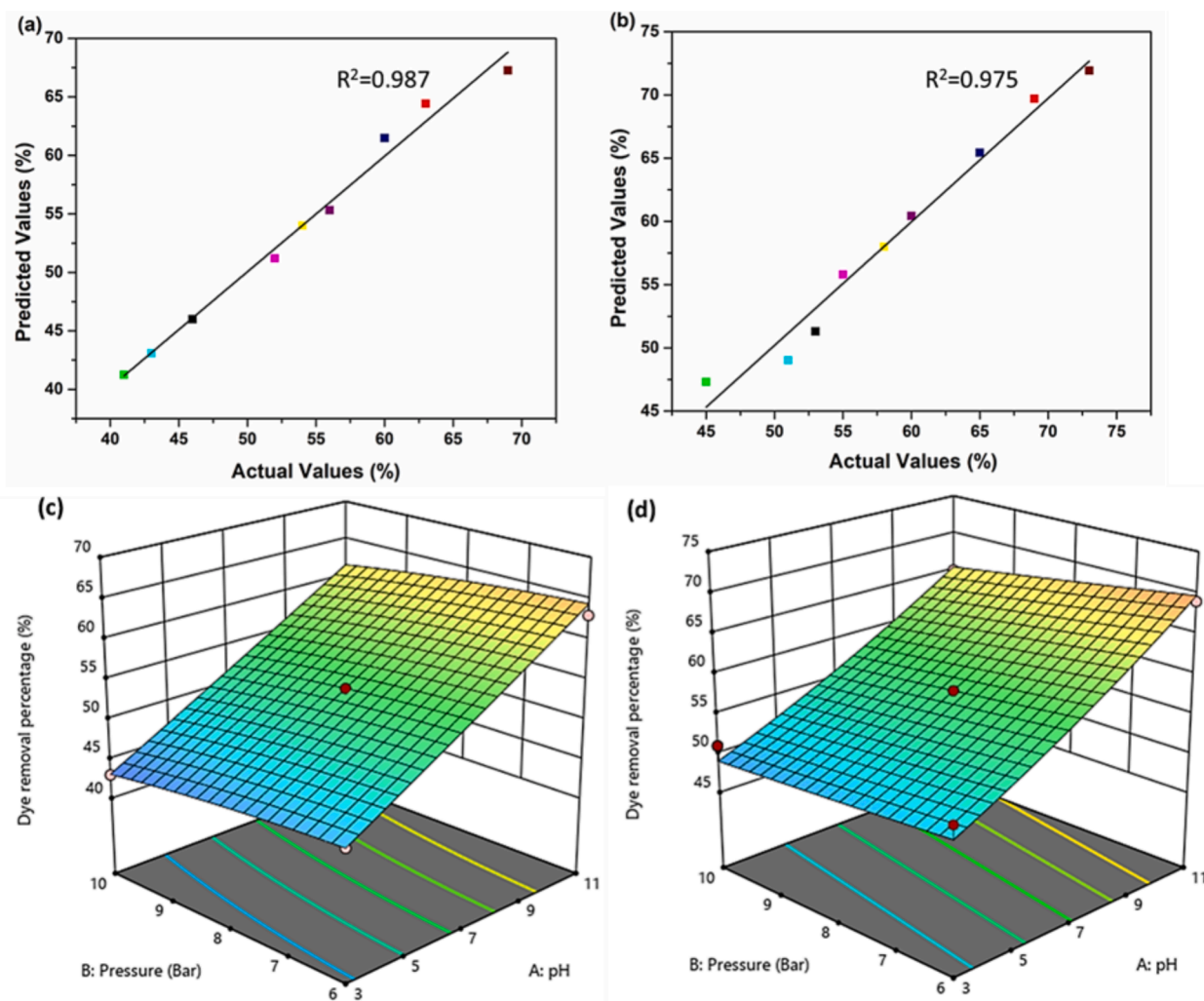| Pollutant	Source	Sum of Squares	df	Mean Square	F-value	p-value	R^2
MO Removal	Model	695.2	5	139.04	82.45	< 0.0001	0.98
	A	677.1	1	677.1	401.5	< 0.0001	
	B	16.99	1	16.99	10.07	0.025	
	AB	0	1	0	0	1	
	A^2	0.088	1	0.088	0.0523	0.828	
	B^2	0.794	1	0.794	0.4709	0.523	
	Residual	8.43	5	1.69			
	Fit Lack	8.43	3	2.81			
	Error	0	2	0			
MB removal	Model	631.76	5	126.35	42.73	0.0004	0.95
	A	605.48	1	605.48	204.78	< 0.0001	
	B	21.36	1	21.36	7.22	0.043	
	AB	1	1	1	0.34	0.586	
	A^2	3.73	1	3.73	1.26	0.313	
	B^2	0.022	1	0.022	0.0075	0.935	
	Residual	14.78	5	2.96			
	Fit Lack	14.78	3	4.93			
	Error	0	2	0			

I.A. Khan et al.

Fig. 10. Predicted vs. experimental values – determination of variance in the removal of (a) MO and (b) MB. Three dimensional plots showing the interaction between pH and pressure on the removal of (c) MO and (d) MB.

Table 5
Optimization and validation via RSM modelling – Summary of MO and MB removal.

Pollutant	pH	Pressure (Bar)	Removal (%) Predicted	Removal (%) Experimental
MO	11	6	64	63
MB	11	6	69	67

Table 6
Comparison of water flux and dye removal efficiencies of various carbon-based PES membranes.

Membrane	Flux (L/m²h)	Dye/pollutant	% Removal	[Ref]
Cu(terephthalate acid (tpa) GO/PES	140	MO MB	60 20	[38]
PES/Functionalized MWCNTs	14	Acid orange	99	[39]
AC Nanoparticles/PES	8	Sulfate Copper	95 97	[50]
PES/GO	13	Sunset yellow Acridine orange	84.9 48.4	[75]
PES/GO-MOF (UiO-66)	15	MO	89	[76]
GO-CuO PES/CA	Not available	MO	58.82	[77]
AC/PES	38	Not available	Not available	[78]
AC-PAA/PES	**54**	**MO** **MB**	**MO 63** **MB 67**	**This work**

form more hydrophilic PAA functional groups. The successful grafting of PAA on AC was confirmed using ATR-FTIR, TGA, SEM, and EDX spectroscopy. Composite PES membranes incorporating PAA-functionalized AC were prepared using phase inversion. Compared to pristine PES membranes, which had a water flux of 30 L/m²h, the composite membranes containing 0.5 wt% AC-PAA had a significantly higher water flux of 54 L/m²h. Additionally, the AC-PAA containing PES membranes demonstrated exceptionally high removal for MO and MB dyes and effective antifouling characteristics with a flux recovery ratio (FRR) of 72 %. For instance, the M5 membrane had the highest water flux of approximately 60 L/m²h at pH 3, which significantly decreased with an increase in solution pH. Conversely, removal of approximately 55 % for MO and 60 % for MB were achieved at a pressure of 6 bar, with slight decrease observed at higher pressures. Experimental results also revealed high removal of 63 % for MO and 67 % for MB at a high solution pH of 11. The combined effects of pH and pressure variations on

the performance of the M5 membrane (0.5 wt% AC-PAA) were investigated using RSM modeling. The results indicated that optimal performance was achieved at a pH of 11 and a pressure of 6 bar. These experimental results, supported by RSM modeling, underscore the potential and future applications of this novel type of antifouling and pH-sensitive membrane.

CRediT authorship contribution statement

Imran Ahmad Khan: Writing – original draft, Methodology, Investigation, Formal analysis, Data curation, Conceptualization. **Kashif Mairaj Deen:** Writing – review & editing, Writing – original draft, Investigation, Formal analysis, Data curation. **Edouard Asselin:** Writing – review & editing, Visualization, Project administration. **Muhammad Yasir:** Writing – original draft, Methodology, Formal analysis, Conceptualization. **Rehan Sadiq:** Writing – review & editing, Project administration. **Nasir M. Ahmad:** Supervision, Funding acquisition, Conceptualization.

Declaration of competing interest

The authors declare that they have no known competing financial interests or personal relationships that could have appeared to influence the work reported in this paper.

Acknowledgments

References

[1] Q. Liu, S. Huang, Y. Zhang, S. Zhao, Comparing the antifouling effects of activated carbon and TiO$_2$ in ultrafiltration membrane development, J. Colloid Interface Sci. 515 (2018) 109–118.

[2] T. Rasheed, M. Bilal, F. Nabeel, M. Adeel, H.M.N. Iqbal, Environmentally-related contaminants of high concern: potential sources and analytical modalities for detection, quantification, and treatment, Environ. Int. 122 (2019) 52–66.

[3] X. Li, et al., Chemical sensing failed by aggregation-caused quenching? A case study enables liquid/solid two-phase determination of N$_2$H$_4$, Chem. Eng. J. 415 (2021) 128975.

[4] M. Tabish, A.B. Tabinda, Z. Mazhar, A. Yasar, J. Ansar, I. Wasif, Physical, chemical and biological treatment of textile wastewater for removal of dyes and heavy metals, Desalin. Water Treat. (2024) 100842.

[5] J.S. Sravan, L. Matsakas, O. Sarkar, Advances in biological wastewater treatment processes: focus on low-carbon energy and resource recovery in biorefinery context, Bioeng (Basel, Switzerland) 11 (2024).

[6] M.-L. Han, et al., A heterometallic sodium–europium-cluster-based metal–organic framework as a versatile and water-stable chemosensor for antibiotics and explosives, J. Mater. Chem. C 5 (33) (2017) 8469–8474.

[7] L. Li, et al., Recent advances in Al(iii)/In(iii)-based MOFs for the detection of pollutants, New J. Chem. 46 (41) (2022) 19577–19592.

[8] Z. Zhou, et al., Oxidative deoximation reaction induced recognition of hypochlorite based on a new fluorescent lanthanide-organic framework, Chem. Eng. J. 351 (2018) 364–370.

[9] X. Zhang, S. Zhang, Y. Tang, X. Huang, H. Pang, Recent advances and challenges of metal–organic framework/graphene-based composites, Compos. Part B Eng. 230 (2022) 109532.

[10] S. Shen, Y.N. Yang, Carbon dioxide absorption into aqueous potassium salt solutions of arginine for post-combustion capture, Energy Fuel 30 (8) (2016) 6585–6596.

[11] E. Shekarian, M.R. Jafari Nasr, T. Mohammadi, O. Bakhtiari, M. Javanbakht, Preparation of 4A zeolite coated polypropylene membrane for lithium-ion batteries separator, J. Appl. Polym. Sci. 136 (32) (2019) 4–14.

[12] A. Marjani, A.T. Nakhjiri, M. Adimi, H.F. Jirandehi, S. Shirazian, Effect of graphene oxide on modifying polyethersulfone membrane performance and its application in wastewater treatment, Sci. Rep. 10 (1) (2020) 1–11.

[13] A.T. Nakhjiri, A. Heydarinasab, O. Bakhtiari, T. Mohammadi, The effect of membrane pores wettability on CO2 removal from CO2/CH4 gaseous mixture using NaOH, MEA and TEA liquid absorbents in hollow fiber membrane contactor, Chinese J. Chem. Eng. 26 (9) (2018) 1845–1861.

[14] A.T. Nakhjiri, A. Heydarinasab, O. Bakhtiari, T. Mohammadi, Influence of non-wetting, partial wetting and complete wetting modes of operation on hydrogen sulfide removal utilizing monoethanolamine absorbent in hollow fiber membrane contactor, Sustain. Environ. Res. 28 (4) (2018) 186–196.

[15] I. Salahshoori, A. Seyfaee, A. Babapoor, Recent advances in synthesis and applications of mixed matrix membranes, Synth. Sinter. 1 (1) (2021) 1–27.

[16] Y.N. Li, H. Li, H. Ye, Y.Z. Zhang, Y. Chen, Preparation and characterization of poly (ether sulfone)/fluorinated silica organic–inorganic composite membrane for sulfur dioxide desulfurization, High Perform. Polym. 31 (1) (2019) 72–85.

[17] P.F. Andrade, A.F. de Faria, S.R. Oliveira, M.A.Z. Arruda, M. do Carmo Gonçalves, Improved antibacterial activity of nanofiltration polysulfone membranes modified with silver nanoparticles, Water Res. 81 (2015) 333–342.

[18] C. Casado-Coterillo, A. Garea, Á. Irabien, Effect of water and organic pollutant in CO2/CH4 separation using hydrophilic and hydrophobic composite membranes, Membranes (Basel) 10 (12) (2020) 1–12.

[19] M.G. Kochameshki, A. Marjani, M. Mahmoudian, K. Farhadi, Grafting of diallyldimethylammonium chloride on graphene oxide by RAFT polymerization for modification of nanocomposite polysulfone membranes using in water treatment, Chem. Eng. J. 309 (2017) 206–221.

[20] M. Cifuentes-Cabezas, C. Carbonell-Alcaina, M.C. Vincent-Vela, J.A. Mendoza-Roca, S. Álvarez-Blanco, Comparison of different ultrafiltration membranes as first step for the recovery of phenolic compounds from olive-oil washing wastewater, Process Saf. Environ. Prot. 149 (2021) 724–734.

[21] T. Xiang, T. Lu, Y. Xie, W.F. Zhao, S.D. Sun, C.S. Zhao, Zwitterionic polymer functionalization of polysulfone membrane with improved antifouling property and blood compatibility by combination of ATRP and click chemistry, Acta Biomater. 40 (2016) 162–171.

[22] I.A. Khan, N.M. Ahmad, Activated carbon, CNTs and GO based polymeric nanocomposites membranes for textile wastewater treatment: preparation, performance, and fouling control, Environ. Sci. Proc. 25 (1) (2023) 77.

[23] M.F. Hassan, M.A. Sabri, H. Fazal, A. Hafeez, N. Shezad, M. Hussain, Recent trends in activated carbon fibers production from various precursors and applications-a comparative review, J. Anal. Appl. Pyrol. 145 (2020) 104715.

[24] S.Z. Naji, C.T. Tye, A review of the synthesis of activated carbon for biodiesel production: precursor, preparation, and modification, Energy Convers. Manag. X 13 (2022) 100152.

[25] I.A. Khan, et al., Ultrasonic assisted removal of methyl orange and bovine serum albumin from wastewater using modified activated carbons: RSM optimization and reusability, Mater. Res. Express 11 (9) (2024) 95505.

[26] P. Barpanda, G. Fanchini, G.G. Amatucci, Structure, surface morphology and electrochemical properties of brominated activated carbons, Carbon n. y. 49 (7) (2011) 2538–2548.

[27] X. Wang, et al., Key factors and primary modification methods of activated carbon and their application in adsorption of carbon-based gases: a review, Chemosphere 287 (P2) (2022) 131995.

[28] B. Cevallos Toledo, R., F. Aragón-Tobar, C., Gámez, S. and de la Torre, E., 2020. Reactivation process of activated carbons: effect on the mechanical and adsorptive properties. Molecules, 25(7), p.1681.

[29] Y. Liu, X. Miao, J. Zhu, Z. Zhang, Z. Cheng, X. Zhu, Polymer-grafted modification of activated carbon by surface-initiated AGET ATRP, Macromol. Chem. Phys. 213 (8) (2012) 868–877.

[30] W. He, H. Jiang, L. Zhang, Z. Cheng, X. Zhu, Atom transfer radical polymerization of hydrophilic monomers and its applications, Polym. Chem. 4 (10) (2013) 2919–2938.

[31] R.K. Layek, A.K. Nandi, A review on synthesis and properties of polymer functionalized graphene, Polymer (Guildf) 54 (19) (2013) 5087–5103.

[32] D.J. Haloi, K. Naskar, N.K. Singha, Modification of chlorinated poly(propylene) via atom transfer radical graft copolymerization of 2-ethylhexyl acrylate: a brush-like graft copolymer, Macromol. Chem. Phys. 212 (5) (2011) 478–484.

[33] S. Chen, L. Li, C. Zhao, J. Zheng, Surface hydration: Principles and applications toward low-fouling/nonfouling biomaterials, Polymer (Guildf) 51 (23) (2010) 5283–5293.

[34] P. Liu, T. Wang, Surface-initiated atom transfer radical polymerization of hydroxyethyl acrylate from activated carbon powder with homogenized surface groups, Surf. Rev. Lett. 14 (2) (2007) 269–275.

[35] A. Demirbas, Agricultural based activated carbons for the removal of dyes from aqueous solutions: a review, J. Hazard. Mater. 167 (1–3) (2009) 1–9.

[36] R. Mukherjee, S. De, Preparation, characterization and application of powdered activated carbon-cellulose acetate phthalate mixed matrix membrane for treatment of steel plant effluent, Polym. Adv. Technol. 27 (4) (2016) 444–459.

[37] M. Peyravi, Preparation of adsorptive nanoporous membrane using powder activated carbon: isotherm and thermodynamic studies, Front. Chem. Sci. Eng. 14 (4) (2020) 673–687.

[38] T.A. Makhetha, R.M. Moutloali, Antifouling properties of Cu(tpa)@GO/PES composite membranes and selective dye rejection, J. Memb. Sci. 554 (January) (2018) 195–210.

[39] J. Lewis, M.A.Q. Al-sayaghi, C. Buelke, A. Alshami, Activated carbon in mixed-matrix membranes, Sep. Purif. Rev. 50 (1) (2021) 1–31.

[40] N. Ghaemi, et al., PES mixed matrix nanofiltration membrane embedded with polymer wrapped MWCNT: fabrication and performance optimization in dye removal by RSM, J. Hazard. Mater. 298 (2015) 111–121.

[41] C. Muthukumar, E. Iype, K. Raju, S. Pulletikurthi, B.G. Prakash Kumar, Sunlight assisted photocatalytic degradation using the RSM-CCD optimized sustainable photocatalyst synthesized from galvanic wastewater, J. Mol. Struct. 1263 (2022) 133194.

[42] C. Muthukumar, J. Panchal, K. Reddy, and P. K. B G, "Synergistic photocatalytic degradation of ciprofloxacin under natural sunlight using hot dip galvanization and medical incineration waste residues," Environ. Pollut., vol. 360, no. August, p. 124692, 2024.

[43] C. Muthukumar, S. Alam, E. Iype, and P. K. B G, "Statistical analysis of photodegradation of methylene blue dye under natural sunlight," Opt. Mater. (Amst)., vol. 122, no. PB, p. 111809, 2021.

[44] C. Muthukumar, P. Saginala, M. Changmai, B.G.P. Kumar, Natural sunlight-driven enhanced abatement of real resin industry wastewater using sludge-derived photocatalyst : potential to generate carbon credits, J. Environ. Chem. Eng. 11 (5) (2023) 111014.

[45] S. Gasemloo, M. Khosravi, M.R. Sohrabi, S. Dastmalchi, P. Gharbani, Response surface methodology (RSM) modeling to improve removal of Cr (VI) ions from tannery wastewater using sulfated carboxymethyl cellulose nanofilter, J. Clean. Prod. 208 (2019) 736–742.

[46] M. Batool, et al., Response surface methodology modeling correlation of polymer composite carbon nanotubes/chitosan nanofiltration membranes for water desalination, ACS ES T Water 3 (5) (2023) 1406–1421.

[47] Z. Hai He, et al., Recycling drinking water treatment sludge in construction and building materials: a review, Sci. Total Environ. 926 (2024) 171513.

[48] N. Sezer, M. Koç, Oxidative acid treatment of carbon nanotubes, Surf. Interfaces 14 (2019) 1–8.

[49] R. Han, S. Zhang, C. Liu, Y. Wang, X. Jian, Effect of NaA zeolite particle addition on poly(phthalazinone ether sulfone ketone) composite ultrafiltration (UF) membrane performance, J. Memb. Sci. 345 (1–2) (2009) 5–12.

[50] S.M. Hosseini, S.H. Amini, A.R. Khodabakhshi, E. Bagheripour, B. Van der Bruggen, Activated carbon nanoparticles entrapped mixed matrix polyethersulfone based nanofiltration membrane for sulfate and copper removal from water, J. Taiwan Inst. Chem. Eng. 82 (2018) 169–178.

[51] M.F. Abid, M.A. Zablouk, A.M. Abid-Alameer, Experimental study of dye removal from industrial wastewater by membrane technologies of reverse osmosis and nanofiltration, J. Environ. Heal. Sci. Eng. 9 (1) (2012) 1–9.

[52] J. Kalmár, G. Lente, I. Fábián, Kinetics and mechanism of the adsorption of methylene blue from aqueous solution on the surface of a quartz cuvette by on-line UV-Vis spectrophotometry, Dye. Pigment. 127 (2016) 170–178.

[53] S. Xie, P. Huang, J.J. Kruzic, X. Zeng, H. Qian, A highly efficient degradation mechanism of methyl orange using Fe-based metallic glass powders, Sci. Rep. 6 (1) (2016) 21947.

[54] M.H. Mahaninia, P. Rahimian, T. Kaghazchi, Modified Activated carbons with amino groups and their copper adsorption properties in aqueous solution, Chinese J. Chem. Eng. 23 (1) (2015) 50–56.

[55] M.A. Abbas, et al., Surface modification of TFC-PA RO membrane by grafting hydrophilic ph switchable poly(Acrylic Acid) brushes, Adv. Polym. Tech. 2020 (2020) 1–12.

[56] R. Mushtaq, et al., Antifouling and flux enhancement of reverse osmosis membrane by grafting poly (3-sulfopropyl methacrylate) brushes, Membranes (Basel) 11 (3) (2021) 1–16.

[57] K. Rambabu, S. Velu, Performance of polyethersulfone membranes modified with low molecular weight polyacrylic acid, Int. J. Chemtech Res. 8 (7) (2015) 413–421.

[58] M. Hadzirun, M. Zubir, M. Abbas, A. Zaini, Twigs - derived activated carbons via - H 3 PO 4 / ZnCl 2 composite activation for methylene blue and congo red dyes removal, Sci. Rep. (2020) 1–17, 0123456789.

[59] S. Compatibilizer *et al.*, "In Situ Nitroxide-Mediated Polymerized Poly (acrylic acid) as a In Situ Nitroxide-Mediated Polymerized Poly (acrylic acid) as a Stabilizer /

[60] Compatibilizer Carbon Nanotube / Polymer Composites," *J. Nanomater.*, no. 2014, pp. 1–12, 2007.

[60] T. Kavitha, I. Kang, S. Park, Poly(acrylic acid)-Grafted Graphene Oxide as an Intracellular Protein Carrier, Langmuir 30 (2014) 402–409.

[61] Z. Xie, W. Guan, F. Ji, Z. Song, Y. Zhao, Production of biologically activated carbon from orange peel and landfill leachate subsequent treatment technology, J. Chem. 2014 (6) (2014) 1–9.

[62] T.-H. Liou, Development of mesoporous structure and high adsorption capacity of biomass-based activated carbon by phosphoric acid and zinc chloride activation, Chem. Eng. J. 158 (2) (2010) 129–142.

[63] N. Bensacia, Removal of heavy metals by homolytically functionalized poly (acrylic acid) with hydroquinone, Int. J. Ind. Chem. 7 (2016) 369–389.

[64] X. Yi, Z. Xu, Y. Liu, X. Guo, M. Ou, X. Xu, Highly efficient removal of uranium(VI) from wastewater by polyacrylic acid hydrogels, RSC Adv. 7 (11) (2017) 6278–6287.

[65] D.L. Vu, J.S. Seo, H.Y. Lee, J.W. Lee, Activated carbon with hierarchical micro-mesoporous structure obtained from rice husk and its application for lithium-sulfur batteries, RSC Adv. 7 (7) (2017) 4144–4151.

[66] X. Yu, et al., Insight into the significant roles of microstructures and functional groups on carbonaceous surfaces for acetone adsorption, RSC Adv. 8 (38) (2018) 21541–21550.

[67] G. Moradi, S. Zinadini, L. Rajabi, Development of nanofiltration PES membranes incorporated with hydrophilic para hydroxybenzoate alumoxane filler for high flux and antifouling property, Chem. Eng. Res. Des. 158 (2020) 148–163.

[68] A. Rahimpour, M. Jahanshahi, S. Khalili, A. Mollahosseini, A. Zirepour, B. Rajaeian, Novel functionalized carbon nanotubes for improving the surface properties and performance of polyethersulfone (PES) membrane, Desalination 286 (2012) 99–107.

[69] H.R. Panchami, A.M. Isloor, A.F. Ismail, Improved hydrophilic and antifouling performance of nanocomposite ultrafiltration zwitterionic polyphenylsulfone membrane for protein rejection applications, J. Nanostructure Chem. 12 (3) (2021) 343–364.

[70] S. Al Aani, C.J. Wright, M.A. Atieh, N. Hilal, Engineering nanocomposite membranes: addressing current challenges and future opportunities, Desalination 401 (2017) 1–15.

[71] S. Kong, M. young Lim, H. Shin, J. H. Baik, and J. C. Lee, "High-flux and antifouling polyethersulfone nanocomposite membranes incorporated with zwitterion-functionalized graphene oxide for ultrafiltration applications," *J. Ind. Eng. Chem.*, vol. 84, pp. 131–140, 2020.

[72] M. Mahmoudian, M.G. Kochameshki, M. Hosseinzadeh, Modification of graphene oxide by ATRP: a pH-responsive additive in membrane for separation of salts, dyes and heavy metals, J. Environ. Chem. Eng. 6 (2) (2018) 3122–3134.

[73] J. Ma, et al., Enhanced adsorptive removal of methyl orange and methylene blue from aqueous solution by alkali-activated multiwalled carbon nanotubes, ACS Appl. Mater. Interfaces 4 (11) (2012) 5749–5760.

[74] T. Sato, K. Makino, S. Tamesue, G. Ishiura, N. Itoh, Preparation and permeation properties of a pH-responsive polyacrylic acid coated porous alumina membrane, Mem 13 (2023) 1–14.

[75] A. Abdel-Karim, et al., High flux and fouling resistant flat sheet polyethersulfone membranes incorporated with graphene oxide for ultrafiltration applications, Chem. Eng. J. 334 (2018) 789–799.

[76] J. Ma, X. Guo, Y. Ying, D. Liu, C. Zhong, Composite ultrafiltration membrane tailored by MOF@GO with highly improved water purification performance, Chem. Eng. J. 313 (2017) 890–898.

[77] G. Natesan, K. Rajappan, GO–CuO nanocomposites assimilated into CA–PES polymer membrane in adsorptive removal of organic dyes from wastewater, Environ. Sci. Pollut. Res. 30 (15) (2023) 42658–42678.

[78] G.S. Prihandana, et al., Preparation and characterization of polyethersulfone/ activated carbon composite membranes for water filtration, Membranes (Basel) 13 (12) (2023).